POLITECNICO DI TORINO
Repository ISTITUZIONALE

Accuracy Evaluation of Higher-Order Structural Theories for Stiffened Beams Using Neural Networks

Original
Accuracy Evaluation of Higher-Order Structural Theories for Stiffened Beams Using Neural Networks / Petrolo, M., Candita, G., Pagani, A., Carrera, E.. - In: AEROTECNICA MISSILI E SPAZIO. - ISSN 0365-7442. - ELETTRONICO. - 105:6(2026), pp. 987-1010. [10.1007/s42496-026-00324-5]

Availability:
This version is available at: 11583/3016269 since: 2026-10-03T13:59:38Z

Publisher:
Springer International Publishing

Published
DOI:10.1007/s42496-026-00324-5

Terms of use:

This article is made available under terms and conditions as specified in the corresponding bibliographic description in the repository

Publisher copyright

(Article begins on next page)

23 October 2026

Aerotecnica Missili & Spazio (2026) 105:987–1010
https://doi.org/10.1007/s42496-026-00324-5

RESEARCH

Accuracy Evaluation of Higher-Order Structural Theories for Stiffened Beams Using Neural Networks

M. Petrolo[1] · G. Candita[1] · A. Pagani[1] · E. Carrera[1]

Received: 14 April 2026 / Revised: 22 May 2026 / Accepted: 11 June 2026 / Published online: 1 July 2026
© The Author(s) 2026

Abstract
This paper presents a machine learning-based surrogate framework for predicting the accuracy of higher-order beam theories in the analysis of isotropic structures with longitudinal stiffeners and transverse ribs. The proposed approach maps the physical and geometric parameters of the beams directly to the accuracy of a selected structural theory, enabling the selection of the minimum set of generalized displacement variables required to achieve the desired accuracy for a given set of input parameters. The training dataset is generated using the Carrera Unified Formulation and comprises combinations of generalized variables stemming from polynomial expansions up to the fourth order. Unlike previous studies, the input space explicitly includes physical cross-sectional parameters, as well as the presence and positions of stringers and ribs. The full dataset, encompassing all combinations of the considered structural theories and cases, comprises millions of analyses; however, accurate predictions are achieved using Deep Neural Networks with only approximately 1% of the full dataset for training. The results show that the proposed surrogate model reliably predicts the accuracy of a structural theory with good generalization capabilities. Concerning the most influential generalized variables, high accuracy in natural frequency prediction is generally achieved when approximately 60% of the fourth-order expansion terms are retained; all second-order terms are essential, while selected third- and fourth-order terms significantly influence the response.

Keywords CUF · Structural theories · Stiffened beams · Neural networks · FEM

1 Introduction

In structural mechanics, reduced-order models, including one- and two-dimensional theories, are used to approximate three-dimensional problems while reducing computational costs. The accuracy of 1D and 2D theories depends on the effectiveness of the generalized variables, and it is problem-dependent; i.e., a set of generalized variables that is effective for a given structural case may not achieve comparable accuracy for different geometries, materials, or loading conditions [1].

Classical beam theories, such as the Euler–Bernoulli Beam Theory (EBBT) [2] and the Timoshenko Beam Theory (TBT) [3, 4] are effective for slender, homogeneous structures, but they may be inaccurate when thin-walled structures are considered, and transverse shear deformation and anisotropy are significant. To address these limitations, various refined and higher-order beam theories have been developed. Examples of well-established approaches for 1D refined theories are the Generalized Beam Theory (GBT) [5] and the Variational Asymptotic Beam Sectional Analysis (VABS) [6].

Higher-order theories have recently been applied to various structural problems. For example, formulations that account for axial force effects have improved the analysis of box and tubular beam–columns [7], and advances in GBT have enabled the analysis of beams with curvilinear open cross-sections [8]. Other studies have focused on procedures to improve the kinematic description of thin-walled

✉ A. Pagani
alfonso.pagani@polito.it

M. Petrolo
marco.petrolo@polito.it

G. Candita
giulio.candita@polito.it

E. Carrera
erasmo.carrera@polito.it

[1] MUL2 Lab, Department of Mechanical and Aerospace Engineering, Politecnico di Torino, Corso Duca Degli Abruzzi 24, 10129 Turin, Italy

beams, such as recursive formulations for box beams and hierarchical strategies for deriving cross-section deformation modes [9, 10], thereby providing a more detailed description of local effects. Higher-order models have also been used for complex structures, such as welded multi-cell sections, functionally graded tubes, and orthotropic or porous beams [11–13]. Extensions to geometrically exact formulations and nonlinear vibration analysis [14–16] contribute to broaden their applicability. Refined one- and two-dimensional structural models are particularly relevant in aerospace applications, where slender, thin-walled components require accurate, computationally efficient formulations. Recent examples include refined beam finite elements for flexible subsonic wings [17], variable-order models for flutter analysis of laminated composite wings [18], coupled structural-aerodynamic formulations for static aeroelasticity [19], and geometrically exact beam models for helicopter composite rotor blades [20].

The present work adopts the Carrera Unified Formulation (CUF) [21] to develop structural theories of arbitrary order. CUF provides a formal framework for handling higher-order generalized variables, governing equations, and Finite Element (FE) matrices. Through the Axiomatic/Asymptotic Method (AAM) [22–24], each variable can be assessed in order to identify the best theories, i.e., the best set of degrees of freedom, for a given structural problem. However, AAM often entails high computational costs because it requires multiple evaluations to assess the effectiveness of each generalized variable. This paper adopts Machine Learning (ML) techniques to alleviate this computational burden.

The application of ML in structural mechanics and FE analysis [25–31] has attracted increasing attention due to its potential to reduce analysis time while maintaining strong predictive capabilities. Stress prediction [32], structural health monitoring [33, 34], and topology optimization [35] are among the many promising applications. In the aerospace field, recent studies have combined ML techniques with beam and shell structural models. Examples include reduced-order Neural Network (NN) models for nonlinear aeroelastic phenomena of composite beams [36], Convolutional Neural Network models for damage detection using FE-generated strain data from composite wings [37].

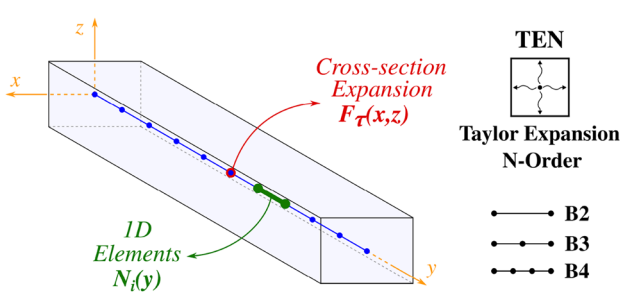

Fig. 1 Beam reference coordinate system

Similar FE-based ML approaches have also been used for multiscale composite wingbox modeling, for example, to predict the response of structures with increased bend-twist coupling using physics-guided neural networks [38]. Moreover, physics-informed neural networks [39] have been developed to enhance NN accuracy by embedding physical laws or parameters into the training process. To further enhance the interpretability of data-driven approaches, explainable machine learning (XML) tools [40] have been introduced and applied in fields such as composite design [41], and damage detection [42].

The present study employs a Deep Neural Network (DNN) [43, 44] to develop a surrogate model that maps the input features, namely structural theories and their generalized variables, and structural parameters describing the beam and its cross-section, to the output, i.e., the accuracy of the natural frequencies. The aim is to identify the optimal set of generalized displacement variables for accurately predicting natural frequencies while minimizing computational cost. By training the network on different structural cases, the proposed AAM–NN framework aims to mitigate the case-dependent nature of the AAM problem and to predict suitable theories for previously unseen configurations, while reducing the computational cost of the purely AAM–FEM-based evaluation of each candidate theory. Given their widespread use in the aerospace sector, structures reinforced with stiffeners and ribs are considered and modeled with 1D theories [45]. In previous works [46–48], ML techniques were used on non-stiffened beam and shell structures to evaluate the relevance of higher-order generalized variables in refined structural theories. In the present study, the beam cross-section is described using physical structural parameters, such as area and inertia moments, which are provided directly as input to the DNN, together with the generalized variables and the positions of stringers and ribs. The focus is on dynamic analyses, which offer advantages over static analyses by simultaneously capturing multiple global structural behaviors—such as bending and torsion. This manuscript is organized as follows: Sect. 2 introduces CUF and presents AAM; Sect. 3 describes the adopted ML approach; Sect. 4 reports the results; and Sect. 5 provides the concluding remarks.

2 Higher-Order Theories and Finite Elements

2.1 Carrera Unified Formulation

Figure 1 shows the reference coordinate system adopted for 1D theories, with the cross-section lying on the x–z plane.

Table 1 Expansion functions

N	M	F_τ
0	1	$F_1 = 1$
1	3	$F_2 = x$ $F_3 = z$
2	6	$F_4 = x^2$ $F_5 = xz$ $F_6 = z^2$
3	10	$F_7 = x^3$ $F_8 = x^2z$ $F_9 = xz^2$ $F_{10} = z^3$
⋮	⋮	⋮
N	(N+1)(N+2)/2	$F_{(N^2+N+2)/2} = x^N$ ... $F_{(N+1)(N+2)/2} = z^N$

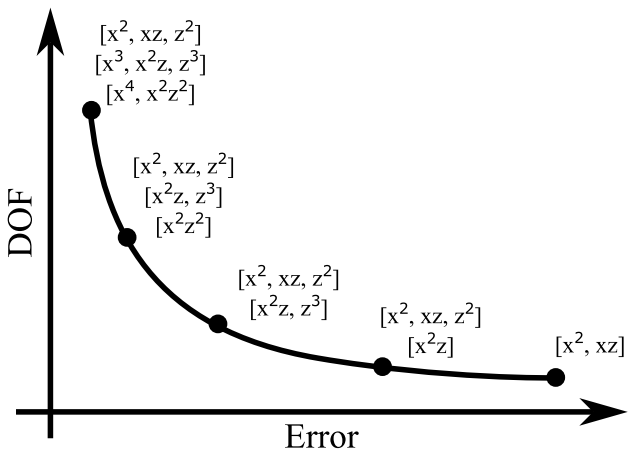

Fig. 2 A Best Theory Diagram (BTD) for 1D theories

The components of the displacement field are defined as follows:

$$\boldsymbol{u}(x,y,z) = \{u_x, u_y, u_z\}^T \tag{1}$$

Within the CUF framework [21], 1D theories express the displacement field and its variation using expansion functions F_τ and F_s:

$$\begin{aligned} &\boldsymbol{u}(x,y,z) = F_\tau(x,z)\boldsymbol{u}_\tau(y) \qquad \delta\boldsymbol{u}(x,y,z) = F_s(x,z)\delta\boldsymbol{u}_s(y) \\ &\tau,\ s=1,\ldots,M \end{aligned} \tag{2}$$

The indexes τ and s denote summation, and M is the number of terms in the expansion. u_τ is the vector of generalized displacement variables. In this work, the expansions are Taylor polynomials, see Table 1.

Models in which the same expansion is used for all three displacement components are referred to as uniform theories. A uniform and full second-order (N = 2) 1D theory has the following displacement field:

$$\begin{aligned} u_x &= u_{x1} + xu_{x2} + zu_{x3} + x^2u_{x4} + xzu_{x5} + z^2u_{x6} \\ u_y &= u_{y1} + xu_{y2} + zu_{y3} + x^2u_{y4} + xzu_{y5} + z^2u_{y6} \\ u_z &= u_{z1} + xu_{z2} + zu_{z3} + x^2u_{z4} + xzu_{z5} + z^2u_{z6} \end{aligned} \tag{3}$$

This theory has eighteen generalized variables or, in an FE model, nodal Degree of Freedom (DOF). Models in which certain terms are omitted from the full expansion are referred to as reduced theories, e.g.,

$$\begin{aligned} u_x &= u_{x1} \\ u_y &= u_{y1} + xu_{y2} + zu_{y3} + x^2u_{y4} + xzu_{y5} + z^2u_{y6} \\ u_z &= u_{z1} + xu_{z2} \end{aligned} \tag{4}$$

The FE formulation is obtained by introducing the shape functions, N_i and N_j,

$$\begin{aligned} &\boldsymbol{u}(x,y,z) = N_iF_\tau\boldsymbol{u}_{\tau i} \qquad \delta\boldsymbol{u}(x,y,z) = N_jF_s\delta\boldsymbol{u}_{sj} \\ &\quad i,\ j=1,\ldots,N_n \end{aligned} \tag{5}$$

N_n is the number of element nodes, while $u_{\tau i}$ and δu_{sj} are the vectors of nodal unknowns and their variations. Further details on the FE formulation can be found in [21, 49]. The Principle of Virtual Displacements (PVD) is employed to derive the governing differential equations,

$$\delta L_{int} = \delta L_{ext} - \delta L_{ine} \tag{6}$$

L_{int} is the strain energy, L_{ext} the work of the external forces, and L_{ine} the work associated with inertial forces. For the free-vibration case, the governing equations are:

$$\delta\boldsymbol{u}_{sj}: \quad \boldsymbol{m}_{\tau sij}\ddot{\boldsymbol{u}}_{\tau i} + k_{\tau sij}\boldsymbol{u}_{\tau i} = 0 \tag{7}$$

$\boldsymbol{k}_{\tau sij}$ and $\boldsymbol{m}_{\tau sij}$ are the fundamental nuclei (FN) of the stiffness and mass matrices, respectively; they are 3× 3 matrices independent of the order of the expansion. The global FE matrices—$\boldsymbol{K}$ and $\boldsymbol{M}$—are obtained by cycling over the four indices τ, s, i, and j. The natural frequencies ω_n and the corresponding modal shapes are determined by solving the eigenvalue problem:

$$(\boldsymbol{K} - \omega_n^2\boldsymbol{M})\boldsymbol{U} = 0 \tag{8}$$

2.2 Axiomatic/Asymptotic Method

The development of structural theories requires selecting the most appropriate expansion terms, namely those that most significantly affect solution accuracy. Different sets of generalized unknown variables, i.e., kinematic assumptions, can be assessed and compared through the AAM. Optimal theory identification is based on selected outputs, such as displacement, stress components, or natural frequencies. One of the AAM outcomes is the Best Theory Diagram (BTD), which, for a fixed number of DOF, shows the set of unknown variables that achieve the highest accuracy, see Fig. 2.

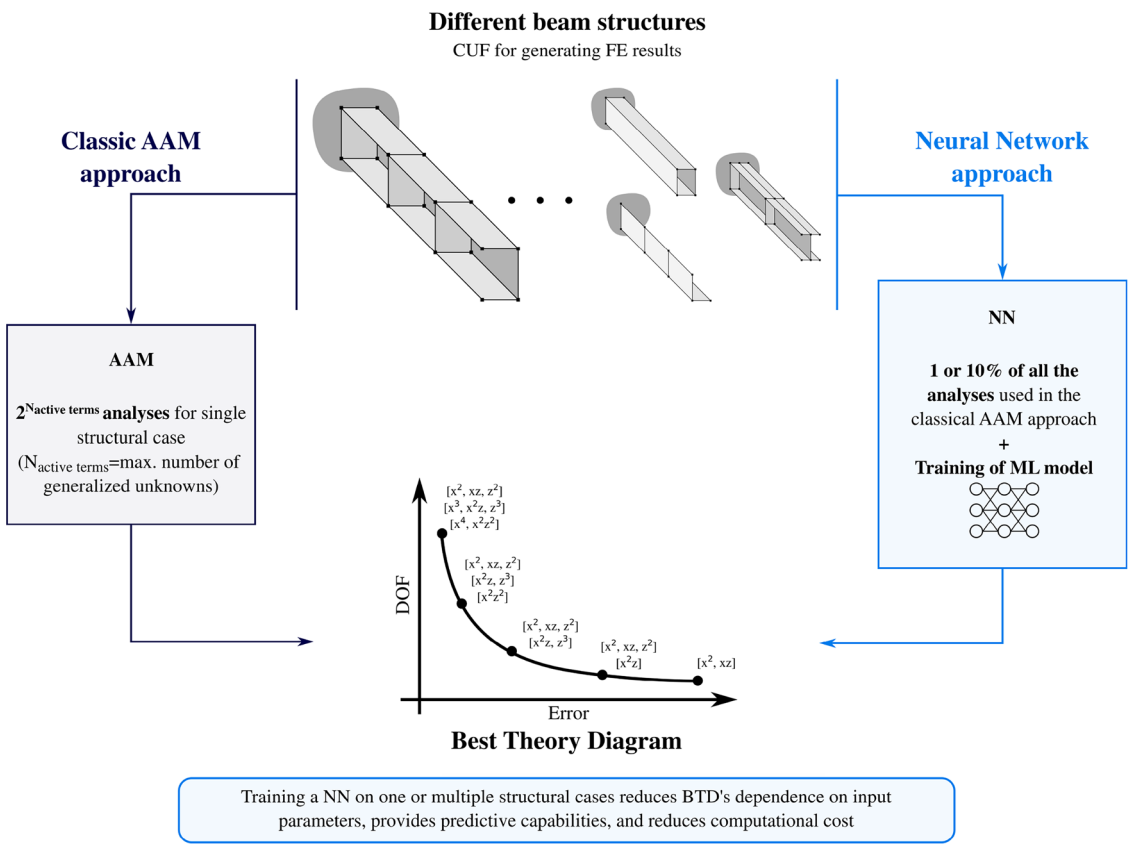

Fig. 3 AAM and DNN approach for developing BTD

Fig. 4 An example of a DNN

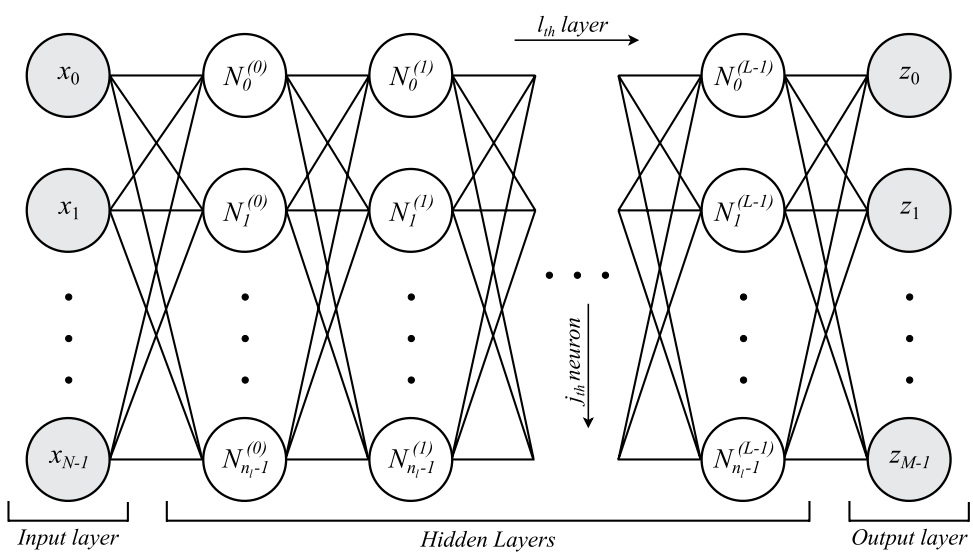

In this work, a full fourth-order, N = 4, Taylor expansion 1D theory is adopted as the reference solution,

$$
\begin{aligned}
u_x &= u_{x1} + x u_{x2} + z u_{x3} + x^2 u_{x4} + \cdots \\
&\quad + x^2 z u_{x8} + \cdots + z^3 u_{x10} + \cdots + x^3 z u_{x12} + \cdots + z^4 u_{x15} \\
u_y &= u_{y1} + x u_{y2} + z u_{y3} + x^2 u_{y4} + \cdots \\
&\quad + x^2 z u_{y8} + \cdots + z^3 u_{y10} + \cdots + x^3 z u_{y12} + \cdots + z^4 u_{y15} \\
u_z &= u_{z1} + x u_{z2} + z u_{z3} + x^2 u_{z4} + \cdots \\
&\quad + x^2 z u_{z8} + \cdots + z^3 u_{z10} + \cdots + x^3 z u_{z12} + \cdots + z^4 u_{z15}
\end{aligned}
\tag{9}
$$

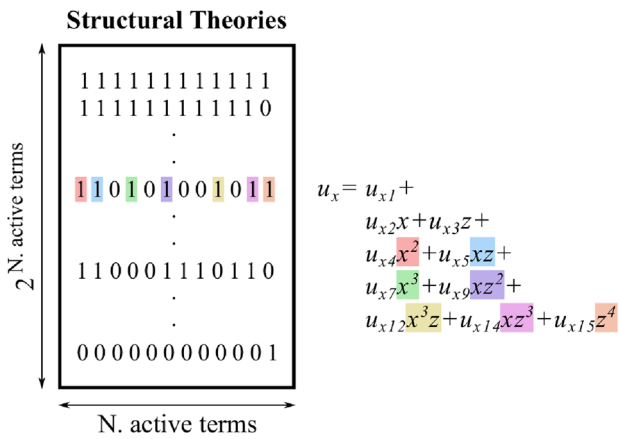

Fig. 5 Input coding for structural theories

Table 2 Beam and cross-section input parameters for DNN

Parameter	Abbreviation
Slenderness ratio	L/h
Cross-section area	A
Inertia moments	I_{xx}, I_{zz}, I_{xz}
Torsional constant	J
x and z shear areas	A_x, A_z
Warping constant	w
Cross-section perimeter	P
x and z neutral axis offsets	X_{NAO}, Z_{NAO}

N = 4 proved to be an optimal candidate for the objectives of this work, as shown in a recent paper [46]; in fact, it enables an effective calculation of the global modes and frequencies for the selected structural cases at a limited computational cost. On the other hand, local modes are not well predicted by such models [21], with Lagrange expansions better suited for those purposes. The accuracy of each theory is evaluated

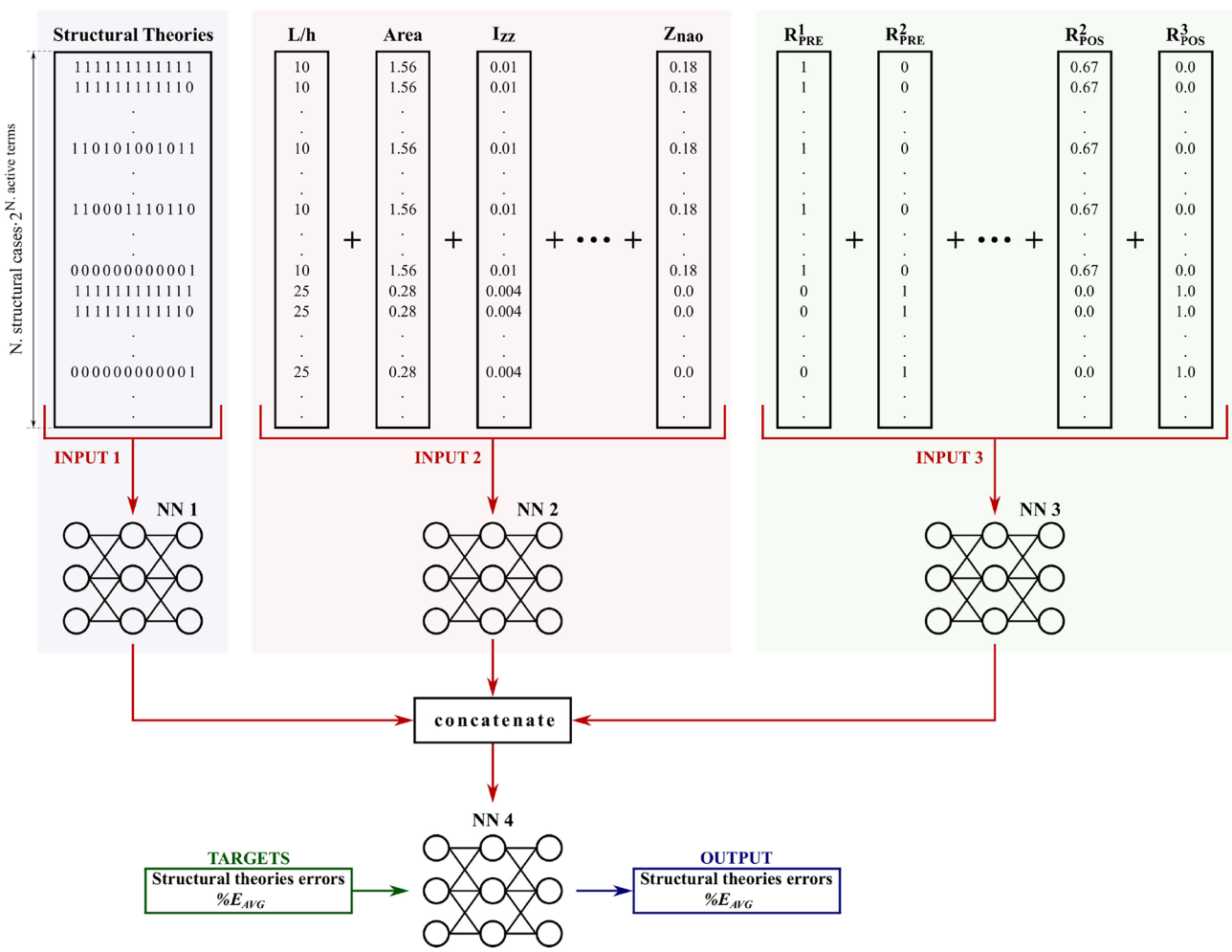

Fig. 6 Global DNN architecture—The model receives three separate inputs: the structural theories encoding, the beam and cross-section properties, and the rib presence/position parameters. Each input is processed by a dedicated branch, and the resulting embeddings are concatenated and fed into a final network that predicts the average error of the first 10 natural frequencies relative to the FE reference solution

using the average percentage relative error $\%E_{AVG}$ computed over the first ten natural frequencies:

$$\%E_{AVG} = 100 \cdot \frac{1}{10} \sum_{i=1}^{10} \frac{\left| f_i - f_i^{N=4} \right|}{\left| f_i^{N=4} \right|} \tag{10}$$

$f_i^{N=4}$ is the i-th natural frequency of the N = 4 theory, and f_i is the corresponding frequency of the theory under evaluation. To develop a BTD, which is strictly linked to a single structural case, the AAM may require a substantial number of numerical analyses, since all possible combinations of expansion terms must be examined; for instance, for an N = 4 1D theory with 15 generalized unknowns per displacement component, 2^{45} analyses are required. Moreover, whenever the problem inputs change, such as the geometry, the entire procedure must be repeated. To reduce this computational burden, different strategies can be adopted. One approach is to exclude specific terms from the selection process by assuming they are always active. This is typically applied to constant and first-order terms, which are known to contribute substantially to meaningful and accurate results. This reduces the number of analyses required to 2^{36}. A second strategy involves activating or deactivating the same expansion terms simultaneously for all three displacement components, thereby reducing the number of required analyses to 2^{12}.

3 Neural Networks

The present paper aims to employ DNN to reproduce the AAM outcome, namely the BTD, using only a limited portion of the analysis required by AAM, as shown in Fig. 3.

Each BTD generated by AAM is strongly problem-dependent; on the other hand, training a DNN on multiple structural cases reduces BTD's dependence on input parameters, provides predictive capabilities, and reduces computational cost. The features of the structural problems, e.g., geometry, material, and boundary conditions, are included in the training phase to allow the DNN to capture the influence of generalized displacements for assigned problem inputs. Neural Networks [50] are designed to learn the behavior of a system and to replicate it after appropriate training. Depending on the data type and the problem, different learning strategies can be adopted [51]. In this study, a supervised learning approach is used, in which the model is trained on labeled datasets to learn the mapping from inputs to outputs. A common example is the fully connected Deep Neural Network (DNN), illustrated in Fig. 4 following the TensorFlow notation. The input vector, x, consists of N elements, the output vector z contains M elements, and each hidden layer is composed of a set of neurons $N_j^{(l)}$, whose number may vary from one layer to another.

Table 3 DNN branches parameters

Branch	Layer type	Layer size	Activation function
1	Dense	32	tanh
	Dense	16	tanh
2	Dense	32	tanh
	Dense	16	tanh
3	Dense	16	tanh
	Dense	8	tanh
Vectors concatenation			
4	Dense	64	tanh
	Dense	32	tanh
	Dense (output)	1	linear

3.1 Neural Network Inputs and Architecture

Within the proposed framework, a structural theory is one of the DNN inputs, in which generalized displacements are encoded as 1 or 0, corresponding to active or inactive terms, respectively, e.g.,

$$\begin{array}{l} u_x = u_{x1} + \quad zu_{x3} \\ u_y = u_{y1} + \quad x^2 u_{y4} + xzu_{y5} \\ u_z = u_{z1} + \quad xu_{z2} + \quad z^2 u_{z6} \end{array} \rightarrow [111\ 001\ 100\ 010\ 010\ 001] \tag{11}$$

Since constant and first-order terms generally play a fundamental role in 1D theories, they are always kept active in the present work. Under this assumption, the total number of possible structural theory combinations is reduced

Table 4 Percentage of theories included in the training dataset for one structural case and different dataset sizes

n	14	13	12	11	10	9	8	7	6	5	4
N_n	12	66	220	495	792	924	792	495	220	66	12
c_n (%)	Dataset 10% - S = 427										
	41.6	22.73	13.63	10.10	9.47	8.33	9.47	10.10	13.63	22.73	41.6
	Dataset 5% - S = 212										
	25.0	15.15	5.91	4.65	3.66	3.25	3.66	4.65	5.91	15.15	25.0
	Dataset 1% - S = 49										
	25.0	4.55	1.82	1.01	0.76	0.76	0.76	1.01	1.82	4.55	25.0
	Dataset 0.3% - S = 11										
	8.33	1.52	0.45	0.20	0.13	0.11	0.13	0.20	0.45	1.52	8.33

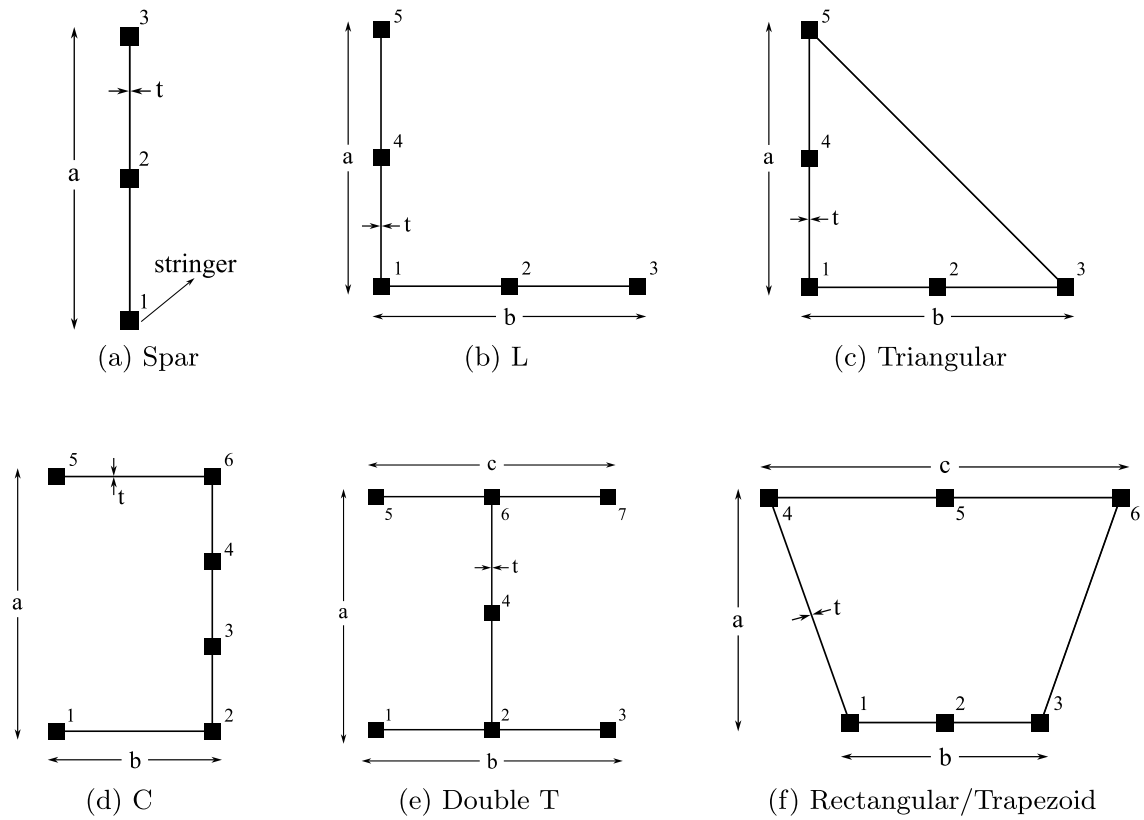

Fig. 7 Reference configurations for the 36 different cross-sections used for the network training

Table 5 Geometry of the cross-sections

Cross-section	Dimensions (cm)	Stringer position
	(a) or (a,b) or (a,b,c)	
C	$(70,30)$-$(80,40)$- $(30,50)$-$(50,50)$- $(70,50)$-$(100,70)$	$(/)$-$(1,2,5,6)$- $(/)$-$(1,2,5,6)$- $(1,2,3,5,6)$-$(1,2,3,4,5,6)$
L	$(30,30)$-$(90,70)$- $(100,80)$-$(40,90)$- $(20,100)$-$(30,100)$	$(1,3,5)$-$(/)$- $(1,3,5)$-$(1,2,3,5)$- $(/)$-$(1,2,3,4,5)$
Spar	(30)-(40)- (50)-(80)- (100)-(100)	$(/)$-$(1,3)$- $(1,2,3)$-$(1,3)$- $(/)$-$(1,2,3)$
Triangular	$(80,20)$-$(30,50)$- $(60,60)$-$(40,70)$- $(60,100)$-$(100,100)$	$(1,3,5)$-$(1,3,5)$- $(/)$-$(1,2,3,4,5)$- $(1,2,3,5)$-$(1,2,3,4,5)$
Double T	$(50,30,100)$-$(60,40,80)$- $(50,50,50)$-$(60,90,90)$- $(70,70,70)$-$(40,80,80)$	$(1,2,3,4,5,6,7)$-$(1,2,3,5,6,7)$- $(1,2,3,5,6,7)$-$(1,2,3,5,6,7)$ $(/)$-$(1,2,3,5,6,7)$
Rectangular/Trapezoid	$(90,100,100)$-$(50,40,40)$- $(100,40,40)$-$(30,70,70)$- $(30,100,100)$-$(40,40,100)$	$(1,3,4,6)$-$(1,3,4,6)$- $(1,3,4,6)$-$(/)$- $(1,2,3,4,5,6)$-$(1,3,4,5,6)$

from 2^{45} to 2^{36}. A further reduction to 2^{12} combinations is achieved by activating or deactivating simultaneously the three expansion terms associated with a given displacement order, i.e.,

$$\begin{aligned} u_x &= \cdots + z^2 u_{x6} + x^2 z u_{x8} + z^3 u_{x10} + x^2 z^2 u_{x13} + z^4 u_{x15} \\ u_y &= \cdots + z^2 u_{y6} + x^2 z u_{y8} + z^3 u_{y10} + x^2 z^2 u_{y13} + z^4 u_{y15} \rightarrow [0\,0\,1\,0\,1\,0\,1\,0\,0\,1\,0\,1] \\ u_z &= \cdots + z^2 u_{z6} + x^2 z u_{z8} + z^3 u_{z10} + x^2 z^2 u_{z13} + z^4 u_{z15} \end{aligned} \tag{12}$$

The first "1" digit corresponds to the third parabolic term u_{x6}, and the last digit refers to the fourth-order term u_{x15}. With the two assumptions above, a 45-DOF theory may be

Table 6 Frequencies of the Double T and Rectangular beams

Cross-section	Frequency (Hz)									
	1st	2nd	3rd	4th	5th	6th	7th	8th	9th	10th
Double T	6.22	7.16	14.71	35.83	36.25	54.22	71.33	91.31	108.42	131.11
Rectangular	2.32	3.57	14.0	21.19	31.36	36.70	54.47	75.08	78.64	93.81

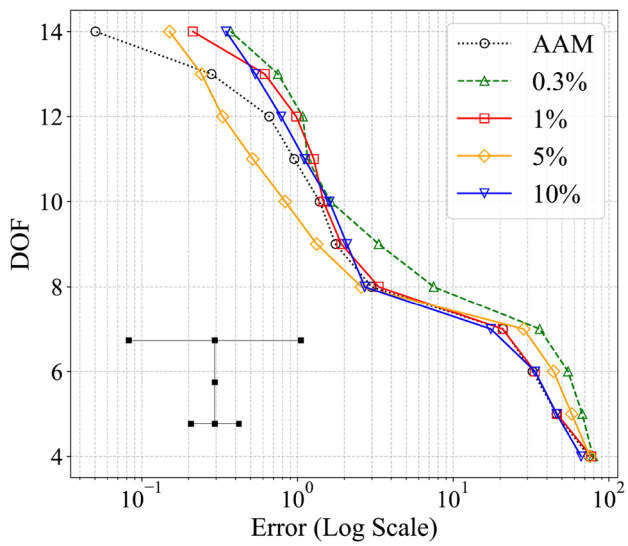

Fig. 8 BTD of the Double T beam from AAM, i.e., the FEM reference, and neural networks with different training dataset sizes—for each DOF level, curve report the minimum error achieved by the structural theories evaluated by FEM or NN

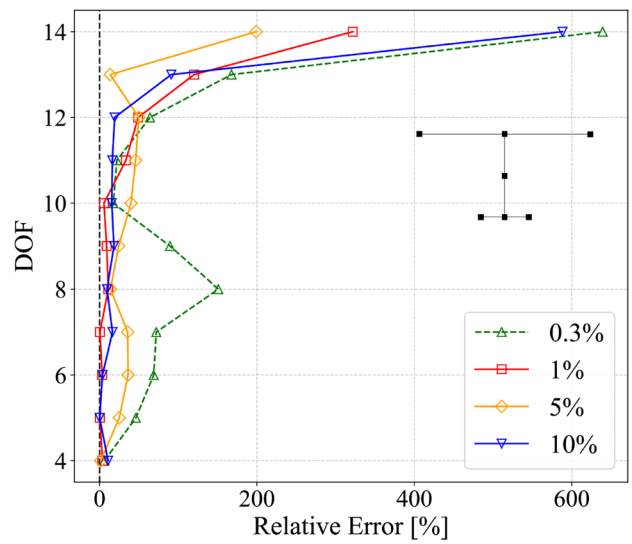

Fig. 9 Relative error of the BTD (in Fig. 8) between those derived from the DNN with different training dataset sizes and that derived from AAM for the Double T cross-section beam

described as a 15-DOF theory. The resulting input matrix, shown in Fig. 5, collects all structural theories for a single structural case. In this study, $N_{\text{active terms}}$–the number of active terms in these theories–is twelve.

The network architecture adopted in this paper, shown in Fig. 6, has multiple inputs. The first is the vector containing the structural theories of all the structural cases. The number of rows is multiplied by $N_{\text{structural case}}$, that is, the number of structural cases considered. In other words, the coding of the theories discussed in the previous section is applied to all structural cases. As explained in the following sections, only a fraction of all possible cases is used for training. The second input includes a combination of beam and cross-section properties, which are listed in Table 2 and were computed in FEMAP. It should be noted that, in this work, the "h" parameter in the L/h ratio is the largest side of the cross-section. The third input concerns the presence of ribs in the beam and their positions along the beam axis. It is coded as an array of six elements, where the first three $(R^1_{PRE}, R^2_{PRE}, R^3_{PRE})$ indicate the presence or absence of ribs, 1 or 0, respectively, and the last three $(R^1_{POS}, R^2_{POS}, R^3_{POS})$ represent the relative position of the ribs along the axis. For instance, the array (1, 0, 1, 0.33, 0.0, 1.0) indicates that there are 2 ribs: the first at 0.33 of the beam length and the second at the tip.

The three inputs are fed into three separate DNN, processing an embedding for each input, and then, concatenated and provided to a final DNN, whose output is the performance parameter from Eq. 10, i.e., the error over the first ten frequencies. During the training phase, the DNN output is compared with FE outputs. Table 3 shows the details of the four branches that compose the DNN.

Different NN depths and widths have been tested here and in previous work [46], and the configuration that yielded reliable results with the smallest depth and width was selected to reduce training computational cost. Increasing the number of layers and neurons has not improved the results, and decreasing them has led to poorer results. Various activation functions have been tested, including "ReLU" and "tanh". The latter proved to be the most accurate. In addition, the Huber loss function and the Adam optimizer were used. The "reduce learning rate on plateau" callback was used. After analyzing the overall trend of the loss function and the prediction quality, the number of epochs was set to 100 to limit training cost.

3.2 Training Dataset Size

According to the assumptions listed previously, for each structural case, there are 2^{12} combinations of structural theories. The aim is to select a fraction of these combinations

Table 7 Best theories from AAM of the Double T beam

DOF	const.	x	z	x^2	xz	z^2	x^3	x^2z	xz^2	z^3	x^4	x^3z	x^2z^2	xz^3	z^4	$\%E_{AVG}$
14	▲	▲	▲	▲	▲	▲	▲	▲	▲	▲	▲	▲	▲	▲	△	5.208E-02
13	▲	▲	▲	▲	▲	▲	△	▲	▲	▲	▲	▲	▲	▲	△	2.212E-01
12	▲	▲	▲	▲	▲	▲	△	△	▲	▲	▲	▲	▲	▲	△	3.527E-01
11	▲	▲	▲	▲	▲	▲	△	▲	▲	▲	△	▲	△	▲	△	4.971E-01
10	▲	▲	▲	▲	▲	▲	△	▲	▲	▲	△	△	△	▲	△	9.957E-01
9	▲	▲	▲	▲	▲	▲	△	△	▲	▲	△	△	△	▲	△	1.727E+00
8	▲	▲	▲	△	▲	▲	△	△	▲	▲	△	△	△	▲	△	3.018E+00
7	▲	▲	▲	△	△	▲	△	△	▲	▲	△	△	△	▲	△	2.902E+01
6	▲	▲	▲	△	▲	△	△	△	▲	△	△	△	△	▲	△	4.040E+01
5	▲	▲	▲	△	△	△	△	△	▲	△	△	△	△	▲	△	5.388E+01
4	▲	▲	▲	△	▲	△	△	△	△	△	△	△	△	△	△	7.862E+01

Table 8 Best theories from DNN of the Double T beam with 0.3% training dataset size

DOF	const.	x	z	x^2	xz	z^2	x^3	x^2z	xz^2	z^3	x^4	x^3z	x^2z^2	xz^3	z^4	$\%E_{AVG}$
14	▲	▲	▲	▲	▲	▲	▲	▲	▲	▲	△	▲	▲	▲	▲	2.274E-01
13	▲	▲	▲	▲	▲	▲	△	▲	▲	▲	▲	▲	▲	▲	△	4.311E-01
12	▲	▲	▲	▲	▲	▲	△	▲	▲	▲	△	▲	▲	▲	△	6.191E-01
11	▲	▲	▲	▲	▲	▲	△	△	▲	▲	△	▲	▲	▲	△	8.532E-01
10	▲	▲	▲	▲	▲	▲	△	△	▲	▲	▲	△	△	▲	△	1.244E+00
9	▲	▲	▲	△	▲	▲	△	▲	▲	▲	△	△	△	▲	△	2.650E+00
8	▲	▲	▲	△	▲	▲	△	△	▲	▲	△	△	△	▲	△	6.777E+00
7	▲	▲	▲	△	△	▲	△	△	▲	▲	△	△	△	▲	△	3.029E+01
6	▲	▲	▲	△	▲	▲	△	△	△	△	△	△	△	△	▲	5.410E+01
5	▲	▲	▲	△	▲	▲	△	△	△	△	△	△	△	△	△	6.760E+01
4	▲	▲	▲	△	▲	△	△	△	△	△	△	△	△	△	△	7.927E+01

Table 9 Best theories from DNN of the Double T beam with 1.0% training dataset size

DOF	const.	x	z	x^2	xz	z^2	x^3	x^2z	xz^2	z^3	x^4	x^3z	x^2z^2	xz^3	z^4	$\%E_{AVG}$
14	▲	▲	▲	▲	▲	▲	▲	▲	▲	▲	△	▲	▲	▲	▲	1.239E-01
13	▲	▲	▲	▲	▲	▲	▲	△	▲	▲	△	▲	▲	▲	▲	2.673E-01
12	▲	▲	▲	▲	▲	▲	△	▲	▲	▲	▲	△	△	▲	▲	3.775E-01
11	▲	▲	▲	▲	▲	▲	△	▲	▲	▲	△	△	△	▲	▲	5.300E-01
10	▲	▲	▲	▲	▲	▲	△	▲	▲	▲	△	△	△	▲	△	8.482E-01
9	▲	▲	▲	▲	▲	▲	△	△	▲	▲	△	△	△	▲	△	1.326E+00
8	▲	▲	▲	△	▲	▲	△	△	▲	▲	△	△	△	▲	△	3.154E+00
7	▲	▲	▲	△	△	▲	△	△	▲	▲	△	△	△	▲	△	2.369E+01
6	▲	▲	▲	△	△	▲	△	△	▲	△	△	△	△	▲	△	4.079E+01
5	▲	▲	▲	△	△	△	△	△	▲	△	△	△	△	▲	△	5.507E+01
4	▲	▲	▲	△	△	△	△	△	△	△	△	△	△	△	▲	8.018E+01

Table 10 Best theories from DNN of the Double T beam with 5.0% training dataset size

DOF	const.	x	z	x^2	xz	z^2	x^3	x^2z	xz^2	z^3	x^4	x^3z	x^2z^2	xz^3	z^4	$\%E_{AVG}$
14	▲	▲	▲	▲	▲	▲	▲	▲	▲	▲	△	▲	▲	▲	▲	1.506E-01
13	▲	▲	▲	▲	▲	▲	▲	▲	▲	▲	△	▲	△	▲	▲	2.419E-01
12	▲	▲	▲	▲	▲	▲	▲	▲	▲	▲	△	△	▲	▲	△	3.300E-01
11	▲	▲	▲	▲	▲	▲	△	▲	▲	▲	△	△	▲	▲	△	5.160E-01
10	▲	▲	▲	▲	▲	▲	△	△	▲	▲	△	△	▲	▲	△	8.332E-01
9	▲	▲	▲	▲	▲	▲	△	△	▲	▲	△	△	△	▲	△	1.327E+00
8	▲	▲	▲	△	▲	▲	△	△	▲	▲	△	△	△	▲	△	2.569E+00
7	▲	▲	▲	△	△	▲	△	△	▲	▲	△	△	△	▲	△	2.834E+01
6	▲	▲	▲	△	△	△	△	△	▲	▲	△	△	△	▲	△	4.410E+01
5	▲	▲	▲	△	△	△	△	△	▲	△	△	△	△	▲	△	5.769E+01
4	▲	▲	▲	△	▲	△	△	△	△	△	△	△	△	△	△	7.542E+01

Table 11 Best theories from DNN of the Double T beam with 10.0% training dataset size

DOF	const.	x	z	x^2	xz	z^2	x^3	x^2z	xz^2	z^3	x^4	x^3z	x^2z^2	xz^3	z^4	$\%E_{AVG}$
14	▲	▲	▲	▲	▲	▲	▲	▲	▲	▲	△	▲	▲	▲	▲	1.609E-01
13	▲	▲	▲	▲	▲	▲	△	▲	▲	▲	▲	▲	▲	▲	△	2.947E-01
12	▲	▲	▲	▲	▲	▲	△	▲	▲	▲	▲	▲	△	▲	△	4.552E-01
11	▲	▲	▲	▲	▲	▲	△	▲	▲	▲	▲	△	△	▲	△	5.846E-01
10	▲	▲	▲	▲	▲	▲	△	△	▲	▲	△	▲	△	▲	△	9.751E-01
9	▲	▲	▲	▲	▲	▲	△	△	▲	▲	△	△	△	▲	△	1.548E+00
8	▲	▲	▲	△	▲	▲	△	△	▲	▲	△	△	△	▲	△	2.410E+00
7	▲	▲	▲	△	△	▲	△	△	▲	▲	△	△	△	▲	△	2.846E+01
6	▲	▲	▲	△	▲	△	△	△	▲	△	△	△	△	▲	△	4.046E+01
5	▲	▲	▲	△	△	△	△	△	▲	△	△	△	△	▲	△	5.372E+01
4	▲	▲	▲	△	△	△	△	△	△	△	△	△	△	▲	△	7.394E+01

to train the DNN. The proper selection must account for the fact that they are not evenly distributed. For example, there are only 12 combinations with 14 DOF, whereas there are 924 with 9 DOF. Such a discrepancy may adversely affect the learning process. To address this issue, different inclusion coefficients are applied to prevent medium-DOF cases from dominating the dataset. The selection process adopts the following coefficients:

$$S_n = c_n \times N_n \tag{13}$$

$$S = \sum_n S_n \tag{14}$$

where n indicates a theory with n-DOF, and S_n is the number of selected samples, c_n is the inclusion coefficient ranging from 0 to 1, and N_n is the total number of available samples. S is the total number of training samples for one structural case. The S_n theories are randomly selected. Table 4 shows the distribution of theories for each n-DOF theory. For example, in the 10% dataset, 427 training samples were used for each structural case. Overall, with 100 structural cases, the training dataset would consist of 42,700 samples.

4 Results

The beams in this work are clamped-free and made of a material with the following characteristics: Young's modulus, E = 75 GPa, Poisson modulus, ν = 0.3, density, ρ = 2700 kg/m^3. Six reference cross-sections were used to develop the dataset for the network training, as shown in Fig. 7. In this work, all cross-sections have a thickness t of 2 mm; the stringers are square with sides of 3 cm; and the ribs are 3 cm thick and solid. Table 5 shows the sets of dimensions adopted for training, resulting in a total of 36 different cross-sections. For instance, in the C section, six combinations of a and b were used to develop six distinct cross-sections with a different number of stringers. In the Table, the column "Stringer position" specifies the position of the stringers, if present, in accordance with the numeration of stringers in Fig. 7. For instance, the C beam with dimensions a = 70 cm, b = 30 cm has 0 stringers (/) , whereas the C beam with a = 40 cm, b = 40 cm has four stringers placed at the corners (1, 2, 5, 6). For cross-sections with three or more stringers on one side, the middle stringers are always equidistant from each other and from the stringers at the corners. Figure 7 shows an example of a C beam with 4 equidistant stringers

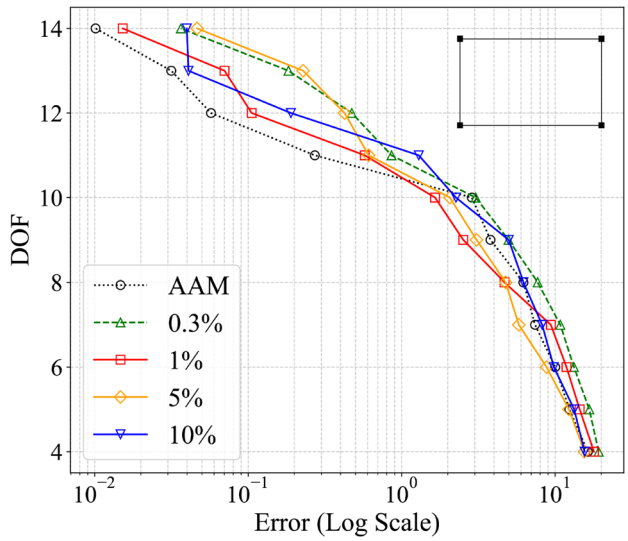

Fig. 10 BTD of the Rectangular beam from AAM and neural networks with different training dataset sizes. For each DOF level, curve report the minimum error achieved by the structural theories evaluated by FEM or NN

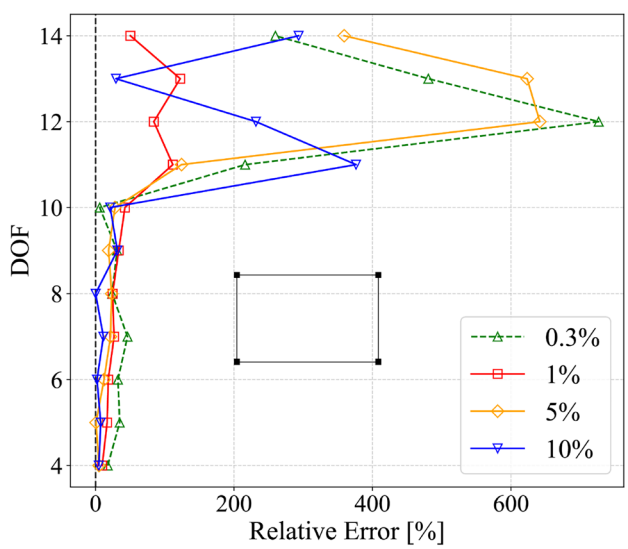

Fig. 11 Relative error of the BTD (in Fig. 10) between those derived from the DNN with different training dataset sizes and that derived from AAM for the Rectangular beam

on the vertical side; furthermore, in the C beam with a = 70 cm, b = 50 cm, and five stringers (1,2,3,5,6), stringer 3 is located in the middle of the vertical side. All beams were analyzed with three lengths—3 m, 5 m, and 10 m—and 8 different rib distributions. In the training dataset, the ribs are placed at three predefined points along the beam: L/3, 2 L/3, and L, with L corresponding to the free tip of the beam. The eight considered rib distributions are defined by all possible combinations of rib locations. Hence, the set includes the case without ribs, the three cases with a single rib, the three cases with two ribs, and the case with three ribs. In the test dataset, which is not included in the training phase, additional rib positions along the beam are considered, distinct from the predefined locations described above. Overall, 864 structural cases were generated, each including 2^{12} structural theory combinations, totaling 3,538,944 FEM modal analyses. A 20 B4 structural mesh was used in all cases, and a B2 element was added for each rib. The structural mesh was chosen based on previous studies and convergence analysis [52, 53], as it provides accurate results for the thin-walled configurations analyzed in this work.

4.1 Selection of the Training Dataset Size

Four dataset sizes were tested: 0.3%, 1%, 5%, and 10%. These percentages refer to the total number of FEM modal analyses (3,538,944). The percentage of theories included in the training dataset is reported in Table 4. The 0.3% dataset corresponds to the case in which, for a given number of DOF, only a combination, or structural theory, is considered, i.e., $S_n = 1, \forall$ n. The results presented hereafter concern two cross-sections: Double T and Rectangular. The latter was not included in the training set and is used to assess the network's ability to extrapolate. The beam configurations are as follows:

- Double T beam: L = 10 m, a = 50 cm, b = 30 cm, c = 100 cm, t = 2 mm, 7 stringers, 0 ribs.
- Rectangular beam: L = 15 m, a = 50 cm, b = 80 cm, c = 80 cm, t = 2 mm, 4 stringers, 3 ribs located at L/3, 2 L/3, and L.

"h" is the largest side of the cross-section between a, b, and c. Table 6 shows the first five frequencies for these structural cases computed using N = 4.

In the following BTD, the error is defined according to Eq. 10: it is evaluated directly from FEM results for the AAM curve, whereas it is predicted by the networks for the DNN curves. Figure 8 shows the BTD of the Double T beam, including the reference AAM curve obtained from all samples and four DNN curves corresponding to different training dataset sizes. This means that only 0.3%, 1%, 5%, and 10% of the 3.5 million FEM modal analyses were effectively used to train the DNN. The relative errors between the BTD obtained from the four DNN trained with different dataset sizes—0.3%, 1%, 5%, and 10%—and that derived from the AAM FEM analyses are reported in Fig. 9. Tables 7, 8, 9, 10, 11 present the best theories from the five sources. Tables 8, 9, 10, 11, corresponding to the different DNN training dataset sizes, include filled and empty red triangles to identify which terms differ with respect to the AAM table. A filled red triangle indicates that the DNN predicted the presence of a generalized variable that is inactive in the

Table 12 Best theories from AAM of the Rectangular beam

DOF	const.	x	z	x^2	xz	z^2	x^3	x^2z	xz^2	z^3	x^4	x^3z	x^2z^2	xz^3	z^4	$\%E_{AVG}$
14	▲	▲	▲	▲	▲	▲	▲	▲	▲	▲	▲	▲	△	▲	▲	1.013E-02
13	▲	▲	▲	▲	▲	▲	▲	▲	▲	▲	△	▲	△	▲	▲	3.154E-02
12	▲	▲	▲	▲	▲	▲	▲	▲	▲	▲	△	▲	△	▲	△	5.727E-02
11	▲	▲	▲	▲	△	▲	▲	▲	▲	▲	△	▲	△	▲	△	2.719E-01
10	▲	▲	▲	▲	△	▲	▲	▲	▲	△	△	▲	△	▲	△	2.867E+00
9	▲	▲	▲	▲	△	△	▲	▲	▲	△	△	▲	△	▲	△	3.794E+00
8	▲	▲	▲	▲	△	△	△	▲	▲	△	△	▲	△	▲	△	6.214E+00
7	▲	▲	▲	△	△	△	△	▲	▲	△	△	▲	△	▲	△	7.402E+00
6	▲	▲	▲	▲	▲	△	△	△	△	△	▲	△	△	△	△	1.003E+01
5	▲	▲	▲	△	▲	▲	△	△	△	△	△	△	△	△	△	1.239E+01
4	▲	▲	▲	△	▲	△	△	△	△	△	△	△	△	△	△	1.636E+01

Table 13 Best theories from DNN of the Rectangular beam with 0.3% training dataset size

DOF	const.	x	z	x^2	xz	z^2	x^3	x^2z	xz^2	z^3	x^4	x^3z	x^2z^2	xz^3	z^4	$\%E_{AVG}$
14	▲	▲	▲	▲	▲	▲	▲	▲	▲	▲	▲	▲	▲	▲	△	3.644E-02
13	▲	▲	▲	▲	▲	▲	▲	▲	▲	▲	△	▲	▲	▲	△	1.831E-01
12	▲	▲	▲	▲	△	▲	△	▲	▲	△	▲	▲	▲	▲	▲	4.734E-01
11	▲	▲	▲	▲	△	▲	△	▲	▲	△	▲	▲	△	▲	▲	8.591E-01
10	▲	▲	▲	▲	△	▲	△	▲	▲	△	△	▲	△	▲	▲	3.040E+00
9	▲	▲	▲	△	△	△	△	▲	▲	▲	▲	▲	△	▲	△	4.974E+00
8	▲	▲	▲	△	△	△	△	▲	▲	▲	△	▲	△	▲	△	7.706E+00
7	▲	▲	▲	△	△	△	▲	▲	▲	△	△	△	△	▲	△	1.082E+01
6	▲	▲	▲	△	△	△	▲	▲	▲	△	△	△	△	△	△	1.327E+01
5	▲	▲	▲	△	△	△	△	▲	△	△	△	△	△	▲	△	1.672E+01
4	▲	▲	▲	△	△	△	△	▲	△	△	△	△	△	△	△	1.924E+01

Table 14 Best theories from DNN of the Rectangular beam with 1.0% training dataset size

DOF	const.	x	z	x^2	xz	z^2	x^3	x^2z	xz^2	z^3	x^4	x^3z	x^2z^2	xz^3	z^4	$\%E_{AVG}$
14	▲	▲	▲	▲	▲	▲	▲	▲	▲	▲	▲	▲	△	▲	▲	1.522E-02
13	▲	▲	▲	▲	▲	▲	▲	▲	▲	▲	▲	▲	△	▲	△	7.011E-02
12	▲	▲	▲	▲	▲	▲	▲	▲	▲	▲	△	▲	△	▲	△	1.054E-01
11	▲	▲	▲	▲	△	▲	▲	▲	▲	▲	△	▲	△	▲	△	5.754E-01
10	▲	▲	▲	▲	△	△	▲	▲	▲	△	△	▲	△	▲	▲	1.651E+00
9	▲	▲	▲	▲	△	△	▲	▲	▲	△	△	▲	△	▲	△	2.522E+00
8	▲	▲	▲	△	△	△	▲	▲	▲	△	△	▲	△	▲	△	4.683E+00
7	▲	▲	▲	▲	△	△	▲	△	▲	△	△	△	△	▲	△	9.386E+00
6	▲	▲	▲	▲	△	△	△	△	▲	△	△	△	△	▲	△	1.187E+01
5	▲	▲	▲	▲	▲	△	△	△	△	△	△	△	△	△	△	1.447E+01
4	▲	▲	▲	△	▲	△	△	△	△	△	△	△	△	△	△	1.792E+01

AAM table; an empty red triangle indicates the opposite. Each row of these tables reports the best theory for a given number of DOF and the corresponding error with respect to the N = 4 structural theory. For instance, the best 6-DOF theory for the Double T cross-section predicted by the AAM is the following:

$$\begin{aligned} u_x &= u_{x1} + xu_{x2} + zu_{x3} + xzu_{x5} + xz^2u_{x9} + xz^3u_{x14} \\ u_y &= u_{y1} + xu_{y2} + zu_{y3} + xzu_{y5} + xz^2u_{y9} + xz^3u_{y14} \\ u_z &= u_{z1} + xu_{z2} + zu_{z3} + xzu_{z5} + xz^2u_{z9} + xz^3u_{z14} \end{aligned} \tag{15}$$

While in the same DOF theory predicted by the 1% DNN, the xz term is replaced by the z^2 highlighted in red:

Table 15 Best theories from DNN of the Rectangular beam with 5.0% training dataset size

DOF	const.	x	z	x^2	xz	z^2	x^3	x^2z	xz^2	z^3	x^4	x^3z	x^2z^2	xz^3	z^4	$\%E_{AVG}$
14	▲	▲	▲	▲	▲	▲	▲	▲	▲	▲	△	▲	▲	▲	▲	4.650E-02
13	▲	▲	▲	▲	▲	▲	▲	▲	▲	▲	▲	▲	△	▲	△	2.281E-01
12	▲	▲	▲	▲	▲	▲	▲	▲	▲	▲	△	▲	△	▲	△	4.247E-01
11	▲	▲	▲	▲	△	▲	▲	▲	▲	▲	△	▲	△	▲	△	6.095E-01
10	▲	▲	▲	△	△	▲	△	▲	▲	▲	▲	▲	△	▲	△	2.061E+00
9	▲	▲	▲	△	△	▲	△	▲	▲	▲	△	▲	△	▲	△	3.077E+00
8	▲	▲	▲	△	△	▲	△	▲	▲	△	△	▲	△	▲	△	4.765E+00
7	▲	▲	▲	△	△	△	△	▲	▲	△	△	▲	△	▲	△	5.804E+00
6	▲	▲	▲	△	△	△	△	▲	▲	△	△	△	△	▲	△	8.800E+00
5	▲	▲	▲	△	▲	△	▲	△	△	△	△	△	△	△	△	1.231E+01
4	▲	▲	▲	△	▲	△	△	△	△	△	△	△	△	△	△	1.553E+01

Table 16 Best theories from DNN of the Rectangular beam with 10.0% training dataset size

DOF	const.	x	z	x^2	xz	z^2	x^3	x^2z	xz^2	z^3	x^4	x^3z	x^2z^2	xz^3	z^4	$\%E_{AVG}$
14	▲	▲	▲	▲	▲	▲	▲	▲	▲	▲	△	▲	▲	▲	▲	3.984E-02
13	▲	▲	▲	▲	▲	▲	▲	▲	▲	▲	△	▲	▲	▲	△	4.084E-02
12	▲	▲	▲	▲	▲	▲	▲	▲	▲	▲	△	▲	△	▲	△	1.899E-01
11	▲	▲	▲	▲	▲	▲	▲	△	▲	▲	△	△	▲	▲	△	1.295E+00
10	▲	▲	▲	▲	▲	▲	▲	△	▲	▲	△	△	△	▲	△	2.261E+00
9	▲	▲	▲	△	▲	▲	▲	△	▲	▲	△	△	△	▲	△	4.991E+00
8	▲	▲	▲	△	▲	▲	△	△	▲	▲	△	△	△	▲	△	6.221E+00
7	▲	▲	▲	▲	▲	▲	▲	△	△	△	△	△	△	△	△	8.239E+00
6	▲	▲	▲	▲	▲	△	▲	△	△	△	△	△	△	△	△	9.820E+00
5	▲	▲	▲	▲	▲	△	△	△	△	△	△	△	△	△	△	1.332E+01
4	▲	▲	▲	△	▲	△	△	△	△	△	△	△	△	△	△	1.558E+01

Table 17 Number of generalized variables in best theories correctly predicted by the DNN for different traing dataset sizes and cross-sections

Dataset size	0.3%	1.0%	5.0%	10.0%
Double T	57/66	58/66	58/66	61/66
Rectangular	48/66	58/66	55/66	48/66

Table 18 Computational time of AAM and DNN with 1% and 10% training dataset sizes

	Dataset creation	Training	Prediction
AAM	∼200 [h]	N/A	N/A
DNN (10%)	∼24 [h]	∼15 [min]	< 1 [s]
DNN (1%)	∼5 [h]	∼2 [min]	< 1 [s]

$$
\begin{aligned}
u_x &= u_{x1} + xu_{x2} + zu_{x3} + z^2u_{x6} + xz^2u_{x9} + xz^3u_{x14} \\
u_y &= u_{y1} + xu_{y2} + zu_{y3} + z^2u_{y6} + xz^2u_{y9} + xz^3u_{y14} \\
u_z &= u_{z1} + xu_{z2} + zu_{z3} + z^2u_{z6} + xz^2u_{z9} + xz^3u_{z14}
\end{aligned}
\tag{16}
$$

Overall, this beam theory has 18 DOF, and the error over the first 10 frequencies relative to the N = 4 theory is 40.4% from the AAM, 40.8% from the 1% DNN. The results concerning the rectangular cross-section are reported in Figs. 10, 11, and Tables 12, 13, 14, 15, 16.

Table 17 shows the number of generalized variables in the best theories correctly predicted by DNN. The total number of variables is the sum of all active variables from second-order to third-order, and from 14 to 4 DOF theories. For instance, with a 10% dataset, the DNN predicted 61 out of 66 generalized variables in the Double T case. Table 18 shows the computational time for the simulations performed with the AAM and the DNN. All simulations were performed on a computer equipped with an "Intel(R) Core(TM) Ultra 7 155 H, 1400 MHz, 16 Core(s), 22 Logical Processor(s)" processor.

The results suggest that:

Table 19 Frequencies of the triangular and L beams

Cross-section	Frequency (Hz)									
	1st	2nd	3rd	4th	5th	6th	7th	8th	9th	10th
Triangular	5.41	9.48	31.73	42.49	53.04	79.79	105.32	118.92	133.61	172.24
L	12.05	26.22	44.80	65.15	76.39	112.50	147.82	154.47	173.64	214.14

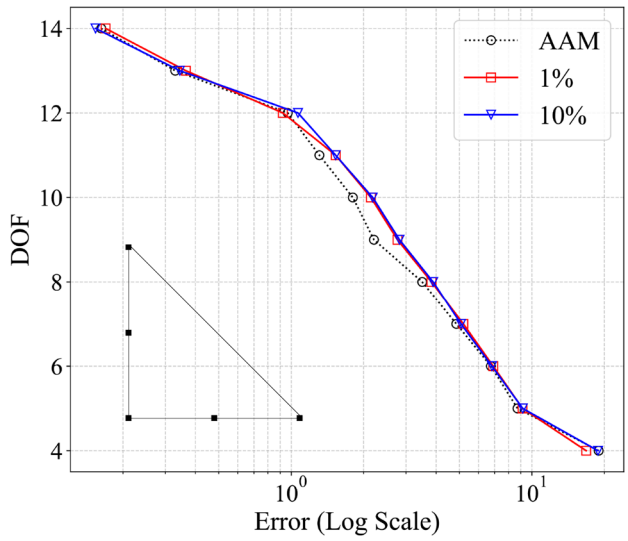

Fig. 12 BTD of the Triangular beam included in the network training. For each DOF level, curve report the minimum error achieved by the structural theories evaluated by FEM or NN

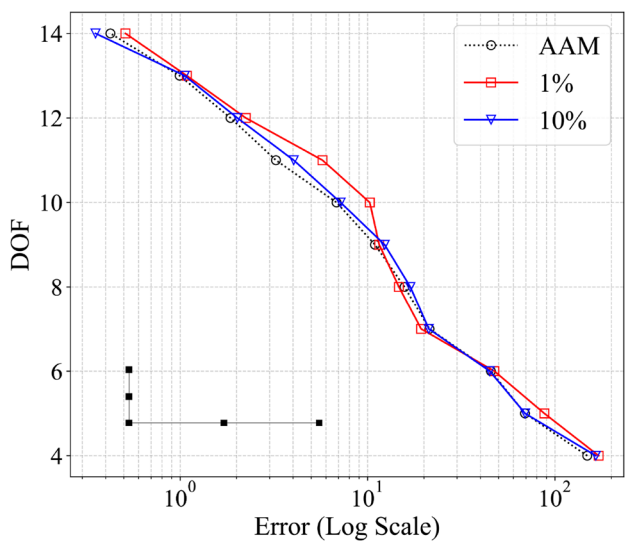

Fig. 13 BTD of the L beam included in the network training. For each DOF level, curve report the minimum error achieved by the structural theories evaluated by FEM or NN

- Overall, the results provided by the DNN are in good agreement with those obtained from the AAM.
- As expected, the use of larger datasets generally leads to predictions that are closer to the AAM results, both in terms of accuracy and in terms of the generalized variables composing the best theories. More significant differences are observed for the rectangular cross-section. Since this cross-section was not included in the training set, the network failed to recover the exact displacement field for most DOF. However, the accuracy of the predicted theories remains high.
- The accuracy of the BTD is satisfactory across all four DNN. The 10% dataset proved most reliable for predicting structural cases in the training set, correctly predicting 61 of 66, whereas the 1% dataset performed best at predicting the optimal theories for previously unseen structural cases, correctly predicting 58 of 66, possibly due to overfitting in the largest dataset. For this reason, only the results for the 1% and 10% datasets are presented in the following sections.
- The relevance of the generalized variables strongly depends on the specific problem, and the network is able to capture these differences across the considered structural cases and the accuracy of the structural theories. For instance, in the Double T beam case, an 8-DOF theory is required to achieve an error below 10%, whereas in the rectangular beam case, a 6-DOF theory is sufficient. Likewise, an error below 0.1% is ensured only by a 14-DOF theory for the Double T beam, while a 12-DOF theory is adequate for the rectangular beam.
- The parabolic and cubic terms are the most frequently activated in both structural cases. In the Double T beam, 61% of the parabolic terms and 59% of the cubic terms are active. Similarly, in the rectangular beam, 61% of the parabolic terms and 52% of the cubic terms are active, with the latter being active from the 7-DOF theory onward. In contrast, for the rectangular beam, the lowest-order theories from 4-DOF to 6-DOF include only parabolic terms, while cubic terms become active only from the 7-DOF theory onward. Fourth-order terms generally appear only in higher-DOF theories, with the exception of the xz^3 term, which is present in all theories from 5-DOF to 14-DOF for the Double T beam. Similarly, for the rectangular beam, where the xz^3 and x^3z terms are almost the only fourth-order contributions active from the 7-DOF theory onward. Furthermore, one term is always inactive in each structural case: z^4 for the Double T beam and x^2z^2 for the rectangular beam.

4.2 Assessment of Neural Network with Beams Included in the Training

This section aims to verify DNN using cases from the training dataset. The results focus on the following cases:

- L beam: L = 3 m, a = 30 cm, b = 100 cm, t = 2 mm, 5 stringers, 2 ribs located at 2 L/3 and L.
- Triangular beam: L = 10 m, a = 100 cm, b = 100 cm, t = 2 mm, 5 stringers, 3 ribs located at L/3, 2 L/3, and L.

Table 20 Best theories from AAM of the Triangular beam

DOF	const.	x	z	x^2	xz	z^2	x^3	x^2z	xz^2	z^3	x^4	x^3z	x^2z^2	xz^3	z^4	$\%E_{AVG}$
14	▲	▲	▲	▲	▲	▲	▲	▲	▲	▲	▲	▲	▲	▲	△	1.624E-01
13	▲	▲	▲	▲	▲	▲	▲	▲	▲	▲	△	▲	▲	▲	△	3.297E-01
12	▲	▲	▲	▲	△	▲	▲	▲	▲	▲	△	▲	▲	▲	△	9.677E-01
11	▲	▲	▲	▲	▲	▲	▲	▲	△	▲	△	▲	▲	△	△	1.309E+00
10	▲	▲	▲	▲	▲	▲	▲	▲	▲	▲	△	△	△	△	△	1.803E+00
9	▲	▲	▲	▲	△	▲	▲	▲	▲	▲	△	△	△	△	△	2.207E+00
8	▲	▲	▲	▲	△	▲	▲	▲	▲	△	△	△	△	△	△	3.503E+00
7	▲	▲	▲	▲	△	▲	△	▲	▲	△	△	△	△	△	△	4.855E+00
6	▲	▲	▲	▲	△	△	△	▲	▲	△	△	△	△	△	△	6.758E+00
5	▲	▲	▲	△	△	△	△	▲	▲	△	△	△	△	△	△	8.719E+00
4	▲	▲	▲	△	△	△	△	△	△	△	△	▲	△	△	△	1.895E+01

Table 21 Best theories from DNN of the Triangular beam with 1.0% training dataset size

DOF	const.	x	z	x^2	xz	z^2	x^3	x^2z	xz^2	z^3	x^4	x^3z	x^2z^2	xz^3	z^4	$\%E_{AVG}$
14	▲	▲	▲	▲	▲	▲	▲	▲	▲	▲	△	▲	▲	▲	▲	1.694E-01
13	▲	▲	▲	▲	▲	▲	▲	▲	▲	▲	△	▲	▲	▲	△	3.649E-01
12	▲	▲	▲	▲	▲	▲	△	▲	▲	▲	△	▲	▲	▲	△	9.233E-01
11	▲	▲	▲	▲	▲	▲	▲	△	▲	▲	△	△	▲	▲	△	1.531E+00
10	▲	▲	▲	▲	▲	▲	▲	▲	▲	▲	△	△	△	△	△	2.143E+00
9	▲	▲	▲	△	▲	▲	▲	▲	▲	▲	△	△	△	△	△	2.763E+00
8	▲	▲	▲	△	△	▲	▲	▲	▲	▲	△	△	△	△	△	3.828E+00
7	▲	▲	▲	△	△	△	▲	▲	▲	▲	△	△	△	△	△	5.191E+00
6	▲	▲	▲	△	△	△	△	▲	▲	▲	△	△	△	△	△	6.911E+00
5	▲	▲	▲	△	△	△	△	▲	▲	△	△	△	△	△	△	9.145E+00
4	▲	▲	▲	△	△	△	△	▲	△	△	△	△	△	△	△	1.681E+01

Table 22 Best theories from DNN of the Triangular beam with 10.0% training dataset size

DOF	const.	x	z	x^2	xz	z^2	x^3	x^2z	xz^2	z^3	x^4	x^3z	x^2z^2	xz^3	z^4	$\%E_{AVG}$
14	▲	▲	▲	▲	▲	▲	▲	▲	▲	▲	△	▲	▲	▲	▲	1.890E-01
13	▲	▲	▲	▲	▲	▲	▲	▲	▲	▲	△	▲	▲	▲	△	5.219E-01
12	▲	▲	▲	▲	▲	▲	▲	△	▲	▲	△	▲	▲	▲	△	9.495E-01
11	▲	▲	▲	▲	▲	▲	▲	△	▲	▲	△	△	▲	▲	△	1.315E+00
10	▲	▲	▲	▲	△	▲	▲	▲	▲	▲	△	△	▲	△	△	1.810E+00
9	▲	▲	▲	▲	△	▲	▲	▲	▲	△	△	△	△	△	▲	2.375E+00
8	▲	▲	▲	▲	△	▲	▲	▲	▲	△	△	△	△	△	△	3.451E+00
7	▲	▲	▲	△	△	▲	▲	▲	▲	△	△	△	△	△	△	4.618E+00
6	▲	▲	▲	▲	△	△	△	▲	▲	△	△	△	△	△	△	6.070E+00
5	▲	▲	▲	△	△	△	△	▲	▲	△	△	△	△	△	△	8.174E+00
4	▲	▲	▲	△	△	△	△	△	△	△	△	▲	△	△	△	1.697E+01

The first five frequencies for these structural cases obtained from the N = 4 theory are shown in Table 19.

Figures 12 and 13 show the BTD for the two cases, obtained using AAM and DNN. Tables 20, 21, 22 show the best theories and their accuracy by AAM and DNN trained with 1% and 10% datasets, for the triangular beam. The L beam results are in Tables 23, 24, 25. The number of correctly predicted generalized variables for both cases and dataset sizes is listed in Table 26.

The results suggest the following:

- The generalized variables composing the best theories are highly consistent when comparing the AAM and DNN results. In other words, the DNN successfully

Table 23 Best theories from AAM of the L beam

DOF	const.	x	z	x^2	xz	z^2	x^3	x^2z	xz^2	z^3	x^4	x^3z	x^2z^2	xz^3	z^4	$\%E_{AVG}$
14	▲	▲	▲	▲	▲	▲	▲	▲	▲	▲	▲	▲	▲	▲	△	4.242E-01
13	▲	▲	▲	▲	▲	△	▲	▲	▲	▲	▲	▲	▲	▲	△	9.933E-01
12	▲	▲	▲	▲	▲	△	▲	▲	▲	△	▲	▲	▲	▲	△	1.857E+00
11	▲	▲	▲	△	▲	△	▲	▲	▲	△	▲	▲	▲	▲	△	3.242E+00
10	▲	▲	▲	△	▲	△	▲	▲	▲	△	△	▲	▲	▲	△	6.829E+00
9	▲	▲	▲	△	△	△	▲	▲	▲	△	▲	▲	▲	△	△	1.095E+01
8	▲	▲	▲	△	△	△	▲	▲	▲	△	△	▲	▲	△	△	1.573E+01
7	▲	▲	▲	△	△	△	▲	▲	▲	△	△	▲	△	△	△	2.137E+01
6	▲	▲	▲	△	△	△	▲	▲	△	△	△	△	△	▲	△	4.549E+01
5	▲	▲	▲	△	△	△	▲	▲	△	△	△	△	△	△	△	6.914E+01
4	▲	▲	▲	△	△	△	△	▲	△	△	△	△	△	△	△	1.485E+02

Table 24 Best theories from DNN of the L beam with 1.0% training dataset size

DOF	const.	x	z	x^2	xz	z^2	x^3	x^2z	xz^2	z^3	x^4	x^3z	x^2z^2	xz^3	z^4	$\%E_{AVG}$
14	▲	▲	▲	▲	▲	▲	▲	▲	▲	▲	▲	▲	▲	▲	△	5.101E-01
13	▲	▲	▲	▲	▲	△	▲	▲	▲	▲	▲	▲	▲	▲	△	1.084E+00
12	▲	▲	▲	▲	▲	▲	▲	▲	▲	△	△	▲	▲	▲	△	2.239E+00
11	▲	▲	▲	▲	▲	▲	▲	▲	▲	△	△	△	▲	▲	△	5.746E+00
10	▲	▲	▲	▲	△	△	▲	▲	▲	▲	△	▲	△	▲	△	1.027E+01
9	▲	▲	▲	△	△	△	▲	▲	▲	△	▲	▲	△	△	▲	1.154E+01
8	▲	▲	▲	△	△	△	▲	▲	▲	△	▲	▲	△	△	△	1.469E+01
7	▲	▲	▲	△	△	△	▲	▲	▲	△	△	▲	△	△	△	1.930E+01
6	▲	▲	▲	△	△	△	▲	▲	△	△	△	▲	△	△	△	4.746E+01
5	▲	▲	▲	△	▲	△	△	△	▲	△	△	△	△	△	△	8.772E+01
4	▲	▲	▲	△	△	△	△	▲	△	△	△	△	△	△	△	1.710E+02

Table 25 Best theories from DNN of the L beam with 10.0% training dataset size

DOF	const.	x	z	x^2	xz	z^2	x^3	x^2z	xz^2	z^3	x^4	x^3z	x^2z^2	xz^3	z^4	$\%E_{AVG}$
14	▲	▲	▲	▲	▲	▲	▲	▲	▲	▲	▲	▲	▲	▲	△	3.891E-01
13	▲	▲	▲	▲	▲	△	▲	▲	▲	▲	▲	▲	▲	▲	△	1.067E+00
12	▲	▲	▲	△	▲	△	▲	▲	▲	▲	▲	▲	▲	▲	△	2.109E+00
11	▲	▲	▲	△	▲	△	▲	▲	▲	△	▲	▲	▲	▲	△	3.574E+00
10	▲	▲	▲	△	▲	△	▲	▲	▲	△	△	▲	▲	▲	△	7.986E+00
9	▲	▲	▲	△	△	△	▲	▲	▲	△	▲	▲	▲	△	△	1.244E+01
8	▲	▲	▲	△	△	△	▲	▲	▲	△	▲	▲	△	△	△	1.608E+01
7	▲	▲	▲	△	△	△	▲	▲	▲	△	△	▲	△	△	△	2.115E+01
6	▲	▲	▲	△	△	△	▲	▲	▲	△	△	△	△	△	△	3.794E+01
5	▲	▲	▲	△	△	△	▲	▲	△	△	△	△	△	△	△	7.755E+01
4	▲	▲	▲	△	△	△	△	▲	△	△	△	△	△	△	△	1.645E+02

Table 26 Number of generalized variables in best theories correctly predicted by the DNN, Triangular and L beam cases

Dataset size	1.0%	10.0%
Triangular	56/66	59/66
L	56/66	63/66

captures the problem features and the influence of the generalized variables on the solution.

- For the triangular beam, both networks correctly predict that at least twelve terms per displacement component are required to keep the error below 1%. For the L-shaped beam, this error threshold is ensured with at least thirteen terms per displacement component.

Table 27 Frequencies of the C and Spar beams

Cross-section	Frequency (Hz)									
	1st	2nd	3rd	4th	5th	6th	7th	8th	9th	10th
C	9.99	11.19	29.73	44.18	61.68	79.32	117.59	141.79	156.65	162.64
Spar	0.44	2.77	5.36	7.78	15.30	15.91	16.31	25.35	27.95	37.95

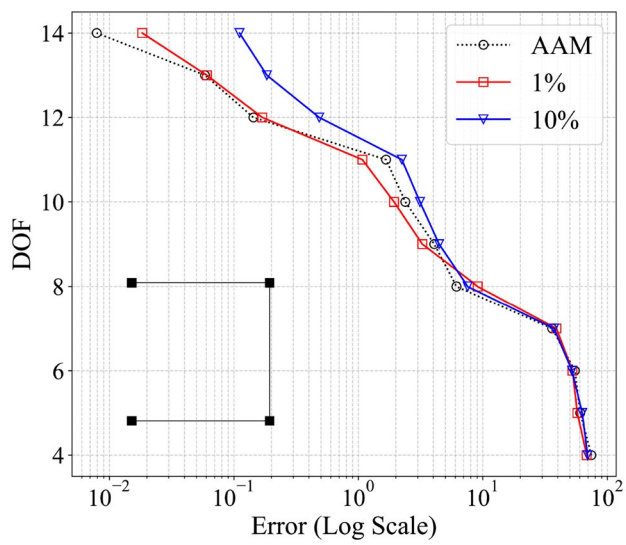

Fig. 14 BTD of the C beam not included in the network training. For each DOF level, curve report the minimum error achieved by the structural theories evaluated by FEM or NN

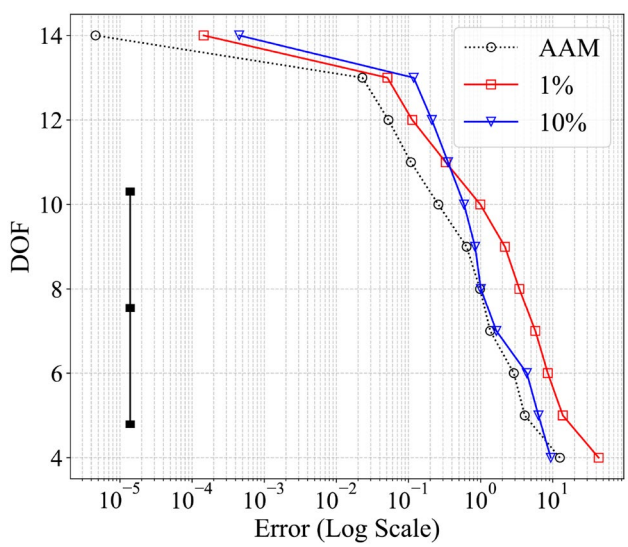

Fig. 15 BTD of the Spar beam not included in the network training. For each DOF level, curve report the minimum error achieved by the structural theories evaluated by FEM or NN

- In both cases, the 1% and 10% networks are capable of predicting errors very close to those obtained with the AAM.
- The parabolic and cubic terms are the most frequently activated in the Triangular beam, with 64% of the parabolic terms and 73% of the cubic terms being active, although fewer of them appear in the lower-order theories. Fourth-order terms appear only from the 11-DOF theory onward, with the exception of the x^3z term, which is present in the 4-DOF theory. In contrast, for the L beam, only 41% of the parabolic terms are active, and they appear only from the 10-DOF theory onward, leaving the lower-order theories without parabolic contributions. In this structural case, the cubic terms are most relevant, with 70% active and distributed across all DOF levels. In particular, the x^3 and x^2z terms are the most influential, being active in almost all theories. These are followed by the fourth-order terms, of which 47% are active.

4.3 Assessment of Neural Network with Beams Not Included in the Training

This section aims to assess the network's performance when applied to structural cases not included in the training set. The results focus on the following cases:

- C beam: L = 7 m, a = 50 cm, b = 50 cm, t = 2 mm, 2 ribs located at L/3 2 L/3.
- Spar beam: L = 8 m, a = 100 cm, t = 2 mm, 1 rib located at 3 L/4.

The first five frequencies for these structural cases obtained by the N = 4 theory are shown in Table 27.

The BTD are shown in Figs. 14 and 15, whereas the best theories are given in Tables 28, 29, 30, 31, 32, 33. Table 34 shows the number of generalized variables in best theories correctly detected by DNN.

The results suggest that:

- The DNN is able to predict the BTD for structural cases not included in the training set. However, the predicted error is less accurate than for the beam cases included in the training phase, although it remains acceptable.
- Depending on the structural case, the accuracy of the generalized variables mapping may vary. The best theories predicted for the C and Spar beam cases are very accurate for both networks trained with 1% and 10% of

Table 28 Best theories from AAM of the C beam

DOF	const.	x	z	x^2	xz	z^2	x^3	x^2z	xz^2	z^3	x^4	x^3z	x^2z^2	xz^3	z^4	$\%E_{AVG}$
14	▲	▲	▲	▲	▲	▲	▲	▲	▲	▲	▲	▲	△	▲	▲	2.452E-02
13	▲	▲	▲	▲	▲	▲	▲	▲	▲	▲	△	▲	△	▲	▲	1.100E-01
12	▲	▲	▲	▲	▲	▲	▲	▲	▲	▲	△	▲	△	▲	△	2.432E-01
11	▲	▲	▲	▲	▲	▲	△	△	▲	▲	▲	▲	△	▲	△	1.951E+00
10	▲	▲	▲	▲	▲	▲	△	△	▲	▲	▲	△	△	▲	△	2.642E+00
9	▲	▲	▲	△	▲	▲	▲	△	▲	▲	△	△	△	▲	△	4.524E+00
8	▲	▲	▲	△	▲	▲	△	△	▲	▲	△	△	△	▲	△	6.719E+00
7	▲	▲	▲	△	△	▲	△	△	▲	▲	△	△	△	▲	△	3.475E+01
6	▲	▲	▲	△	▲	▲	△	△	△	▲	△	△	△	△	△	5.310E+01
5	▲	▲	▲	△	△	▲	△	△	△	▲	△	△	△	△	△	5.836E+01
4	▲	▲	▲	△	△	△	△	△	△	△	▲	△	△	△	△	7.392E+01

Table 29 Best theories from DNN of the C beam with 1.0% training dataset size

DOF	const.	x	z	x^2	xz	z^2	x^3	x^2z	xz^2	z^3	x^4	x^3z	x^2z^2	xz^3	z^4	$\%E_{AVG}$
14	▲	▲	▲	▲	▲	▲	▲	▲	▲	▲	▲	▲	△	▲	▲	1.835E-02
13	▲	▲	▲	▲	▲	▲	▲	▲	▲	▲	△	▲	△	▲	▲	6.060E-02
12	▲	▲	▲	▲	▲	▲	▲	▲	▲	▲	△	▲	△	▲	△	1.690E-01
11	▲	▲	▲	▲	▲	▲	△	▲	▲	▲	△	▲	△	▲	△	1.077E+00
10	▲	▲	▲	△	▲	▲	△	△	▲	▲	▲	▲	△	▲	△	1.932E+00
9	▲	▲	▲	△	▲	▲	△	△	▲	▲	▲	△	△	▲	△	3.260E+00
8	▲	▲	▲	△	▲	▲	△	△	▲	▲	△	△	△	▲	△	9.086E+00
7	▲	▲	▲	△	△	▲	△	△	▲	▲	△	△	△	▲	△	3.899E+01
6	▲	▲	▲	△	△	▲	△	▲	△	△	△	△	△	△	▲	5.242E+01
5	▲	▲	▲	△	△	▲	△	△	△	△	△	△	△	△	▲	5.741E+01
4	▲	▲	▲	△	△	△	△	▲	△	△	△	△	△	△	△	6.820E+01

Table 30 Best theories from DNN of the C beam with 10.0% training dataset size

DOF	*const.*	x	z	x^2	xz	z^2	x^3	x^2z	xz^2	z^3	x^4	x^3z	x^2z^2	xz^3	z^4	$\%E_{AVG}$
14	▲	▲	▲	▲	▲	▲	▲	▲	▲	▲	▲	▲	△	▲	▲	1.109E-01
13	▲	▲	▲	▲	▲	▲	▲	▲	▲	▲	△	▲	△	▲	▲	1.840E-01
12	▲	▲	▲	▲	▲	▲	▲	▲	▲	▲	△	▲	△	▲	△	4.845E-01
11	▲	▲	▲	△	▲	▲	▲	△	▲	▲	▲	▲	△	▲	△	2.234E+00
10	▲	▲	▲	▲	▲	▲	△	△	▲	▲	△	▲	△	▲	△	3.122E+00
9	▲	▲	▲	▲	▲	▲	△	△	▲	▲	△	△	△	▲	△	4.449E+00
8	▲	▲	▲	△	▲	▲	△	△	▲	▲	△	△	△	▲	△	7.542E+00
7	▲	▲	▲	△	△	▲	△	△	▲	▲	△	△	△	▲	△	3.726E+01
6	▲	▲	▲	△	▲	▲	△	△	△	▲	△	△	△	△	△	5.203E+01
5	▲	▲	▲	△	△	▲	△	△	△	▲	△	△	△	△	△	6.280E+01
4	▲	▲	▲	▲	△	△	△	△	△	△	△	△	△	△	△	6.940E+01

the dataset. In fact, the C beam is characterized by a length L not present in the training dataset, whereas the Spar section has a different L and a different rib position. By contrast, the rectangular beam discussed previously has a length L that differs substantially from those used during training and a different cross-sectional geometry, leading to a less accurate mapping of the generalized variables than in the other two cases.

- The AAM and both DNN indicate that at least twelve terms per displacement component are required to keep the error below 1% in the C case. For the Spar case, according to the AAM, only 8 terms are required to maintain the error below 1%, whereas the DNN is more conservative, indicating that 9 and 10 displacement components are necessary for the 10% and 1% DNN, respectively, to satisfy this requirement.

Table 31 Best theories from AAM of the Spar beam

DOF	const.	x	z	x^2	xz	z^2	x^3	x^2z	xz^2	z^3	x^4	x^3z	x^2z^2	xz^3	z^4	$\%E_{AVG}$
14	▲	▲	▲	▲	▲	▲	▲	▲	▲	▲	△	▲	▲	▲	▲	4.587E-06
13	▲	▲	▲	▲	▲	▲	△	▲	▲	▲	△	▲	▲	▲	▲	2.292E-02
12	▲	▲	▲	▲	▲	▲	△	▲	▲	▲	△	△	▲	▲	▲	5.269E-02
11	▲	▲	▲	▲	▲	▲	△	▲	▲	▲	△	△	△	▲	▲	1.079E-01
10	▲	▲	▲	▲	▲	▲	△	▲	▲	△	△	△	△	▲	▲	2.592E-01
9	▲	▲	▲	▲	▲	▲	△	△	▲	△	△	△	△	▲	▲	6.390E-01
8	▲	▲	▲	▲	▲	▲	△	▲	▲	△	△	△	△	△	△	9.804E-01
7	▲	▲	▲	▲	▲	▲	△	△	▲	△	△	△	△	△	△	1.355E+00
6	▲	▲	▲	▲	▲	▲	△	△	△	△	△	△	△	△	△	2.882E+00
5	▲	▲	▲	▲	▲	△	△	△	△	△	△	△	△	△	△	4.085E+00
4	▲	▲	▲	△	▲	△	△	△	△	△	△	△	△	△	△	1.254E+01

Table 32 Best theories from DNN of the Spar beam with 1.0% training dataset size

DOF	const.	x	z	x^2	xz	z^2	x^3	x^2z	xz^2	z^3	x^4	x^3z	x^2z^2	xz^3	z^4	$\%E_{AVG}$
14	▲	▲	▲	▲	▲	▲	▲	▲	▲	▲	△	▲	▲	▲	▲	1.447E-04
13	▲	▲	▲	▲	▲	▲	▲	▲	▲	▲	△	▲	△	▲	▲	5.088E-02
12	▲	▲	▲	▲	▲	▲	▲	▲	▲	▲	△	△	△	▲	▲	1.128E-01
11	▲	▲	▲	▲	▲	▲	△	▲	▲	▲	△	△	△	▲	▲	3.281E-01
10	▲	▲	▲	▲	▲	▲	△	▲	▲	▲	△	△	△	▲	△	9.892E-01
9	▲	▲	▲	▲	▲	▲	△	△	▲	△	△	△	△	▲	▲	2.171E+00
8	▲	▲	▲	▲	▲	▲	△	▲	▲	△	△	△	△	△	△	3.438E+00
7	▲	▲	▲	▲	▲	▲	▲	△	△	△	△	△	△	△	△	5.724E+00
6	▲	▲	▲	▲	▲	▲	△	△	△	△	△	△	△	△	△	8.534E+00
5	▲	▲	▲	▲	▲	△	△	△	△	△	△	△	△	△	△	1.377E+01
4	▲	▲	▲	△	▲	△	△	△	△	△	△	△	△	△	△	4.325E+01

Table 33 Best theories from DNN of the Spar beam with 10.0% training dataset size

DOF	const.	x	z	x^2	xz	z^2	x^3	x^2z	xz^2	z^3	x^4	x^3z	x^2z^2	xz^3	z^4	$\%E_{AVG}$
14	▲	▲	▲	▲	▲	▲	▲	▲	▲	▲	△	▲	▲	▲	▲	4.494E-04
13	▲	▲	▲	▲	▲	▲	▲	▲	▲	▲	△	▲	△	▲	▲	1.179E-01
12	▲	▲	▲	▲	▲	▲	△	▲	▲	▲	△	△	▲	▲	▲	2.105E-01
11	▲	▲	▲	▲	▲	▲	△	▲	▲	▲	△	△	△	▲	▲	3.532E-01
10	▲	▲	▲	▲	▲	▲	△	△	▲	▲	△	△	△	▲	▲	5.883E-01
9	▲	▲	▲	▲	▲	▲	△	▲	▲	▲	△	△	△	△	△	8.375E-01
8	▲	▲	▲	▲	▲	▲	△	▲	▲	△	△	△	△	△	△	1.006E+00
7	▲	▲	▲	▲	▲	▲	△	△	▲	△	△	△	△	△	△	1.649E+00
6	▲	▲	▲	▲	▲	▲	△	△	△	△	△	△	△	△	△	4.365E+00
5	▲	▲	▲	▲	▲	△	△	△	△	△	△	△	△	△	△	6.333E+00
4	▲	▲	▲	△	▲	△	△	△	△	△	△	△	△	△	△	9.373E+00

Table 34 Number of generalized variables correctly predicted by the DNN, C and Spar beam cases

Dataset size	1.0%	10.0%
C	59/66	62/66
Spar	62/66	62/66

- The C and Spar beam cases have a similar distribution of generalized variables. In both cases, the parabolic terms are active in most best theories. The cubic and fourth-order terms are less relevant than the parabolic ones in both cases. In the C beam, 57% of the cubic terms and 33% of the fourth-order terms are active, while these percentages decrease to 43% and 31%, respectively, in the Spar beam.

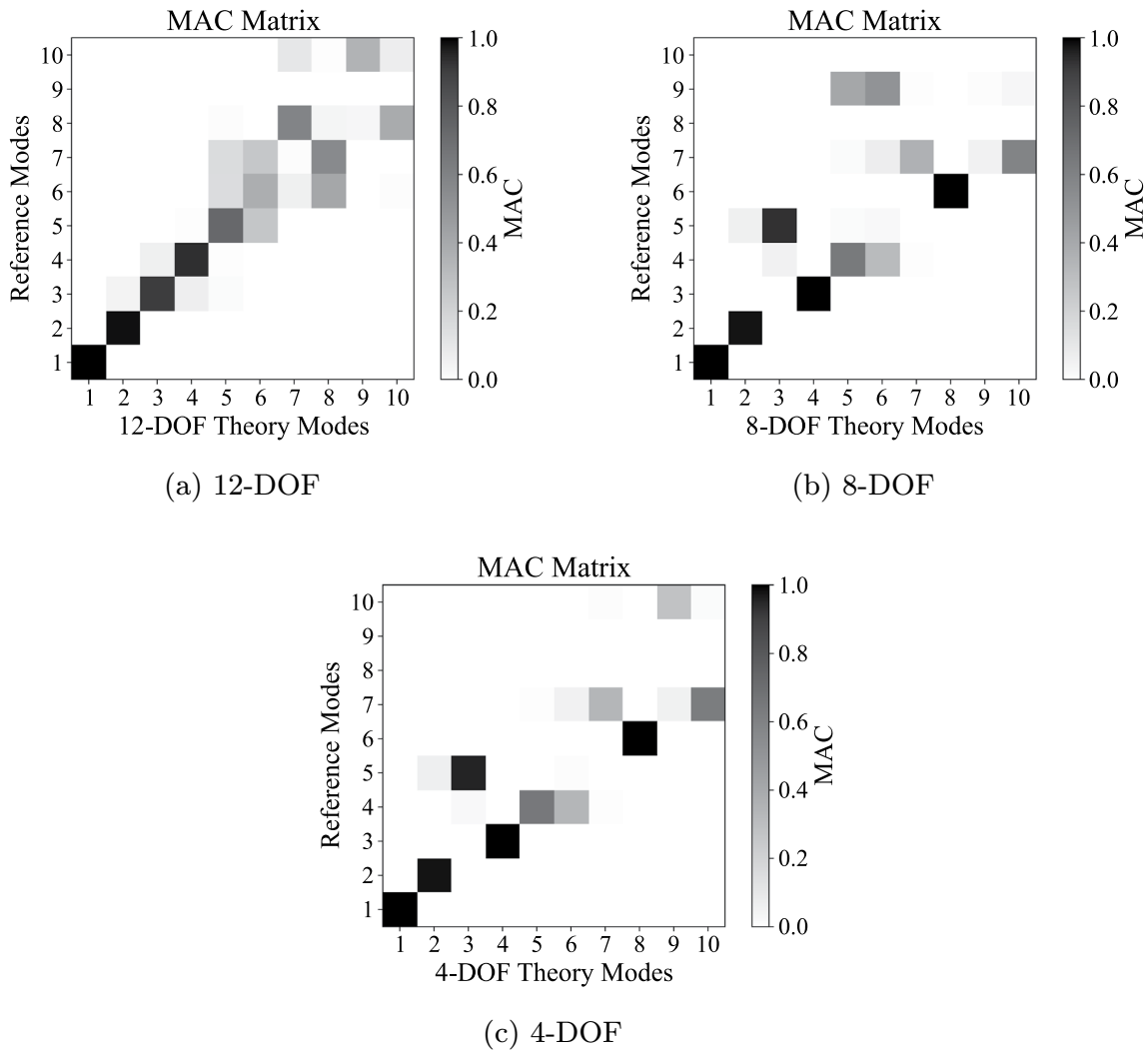

Fig. 16 MAC matrix for the Double T beam to quantify the matching of mode shapes obtained from the two structural theories, with values close to 1 indicating strong agreement between the modes

4.4 Modal Shapes from Best Theories

The best theories were constructed by using the natural frequencies to evaluate their accuracy. This section aims to further assess their reliability by also accounting for the modal shapes. The best theories analyzed in this section are those derived from the DNN trained with 1% of the training dataset. The structural cases considered are the Double T and Rectangular cross-sections discussed in the previous sections. The Modal Assurance Criterion (MAC) [54, 55] was used to compare modal shapes from the best theories and the reference one from the N = 4 theory. The MAC quantifies the correlation between mode shapes obtained from the two structural theories, with values close to 1 indicating strong agreement between the modes.

Figures 16 and 17 show the MAC matrices for the Double T and Rectangular beams, respectively, comparing the reference solution with the best theories including 12, 8, and 4 terms. As expected, increasing the number of DOF leads to progressive convergence of the solution towards the reference one. However, significant differences in the MAC matrices may occur depending on the geometry. In the Double T case, the best 4-DOF theory matches only the first two modes of the reference solution, whereas the higher-order 12-DOF theory ensures a good match for the first four modes. For the Rectangular beam, where the 4-DOF structural theory is able to reproduce almost all modal shapes, except for an inversion between the fifth and sixth modes, indicating that, in the rectangular case, lower-order theories already capture most of the beam's modal behavior.

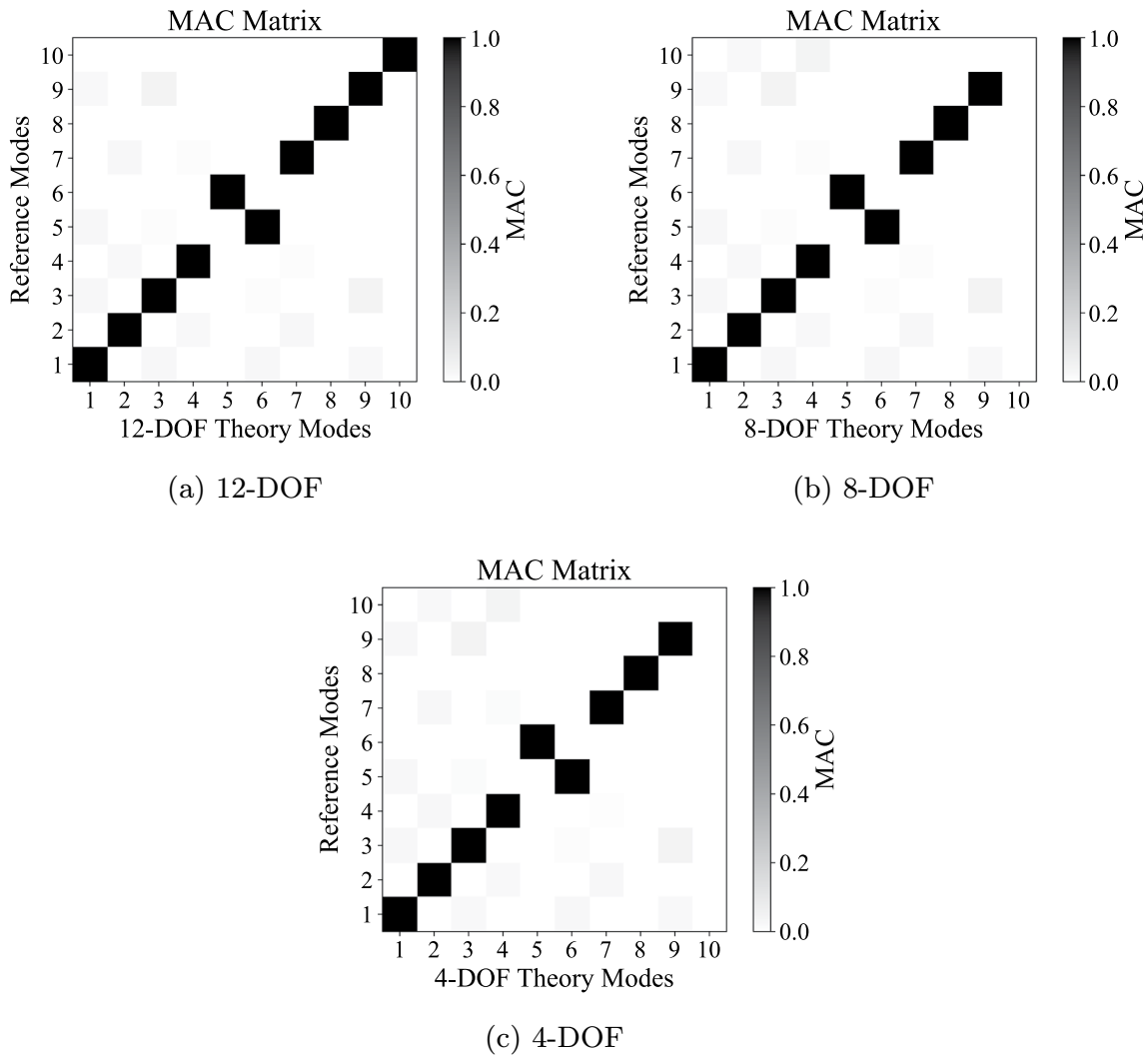

Fig. 17 MAC matrix for the Rectangular beam—It quantifies the correlation between mode shapes obtained from the two structural theories, with values close to 1 indicating strong agreement between the modes

5 Conclusions

This paper proposes a methodology for mapping beam features to higher-order generalized displacement variables. The aim is to provide a tool capable of estimating the accuracy of a beam theory for a given problem and determining the minimum number of DOF required to obtain reliable results. The proposed methodology employs a Deep Neural Network (DNN) to correlate structural theories, geometries, structural parameters, and accuracy. In particular, three Neural Networks (NN) process three distinct input sets, generating embeddings that are subsequently concatenated and fed into a fourth DNN trained on the accuracy values of the structural theories. The training dataset is generated using CUF, which provides FEM solutions for beam theories of arbitrary order. Refined beam theories are obtained by considering a reference fourth-order Taylor expansion and different combinations of the terms composing the full expansion. The accuracy is evaluated considering the natural frequencies of the structure, and various beam and cross-sectional geometries are considered. The results are validated against a comprehensive set of FEM analyses encompassing all samples and structural cases. Meanwhile, the network is trained and tested on different percentages of the dataset; 1% and 10% are selected to present results for the complete dataset. The following conclusions can be drawn:

- Overall, the proposed methodology provides satisfactory results when compared with FEM analyses. With only 1% to 10% of the computational cost of FEM, good agreement is achieved in both accuracy and the mapping of the generalized variables.

- The accuracy predicted by the network shows excellent agreement in all cases. In other words, the network can estimate the accuracy of a given structural theory for a specified beam geometry.
- The network performance in identifying the most relevant generalized variables strongly depends on the structural case considered. In general, the network trained on 1% of the full dataset is more effective at predicting the best theories for structural cases not included in the training set, whereas the 10% network performs better on cases included in the training set.
- In most cases, at least ten generalized variables per displacement component are required to achieve errors below 1%, except for the spar beam, for which the best 8-DOF theory is sufficient. The constant, linear, and parabolic terms are necessary, and selected cubic and fourth-order terms must also be included.

Although this paper focuses on natural frequencies and global modes, the proposed methodology can be adapted to different structural problems. For example, in a static analysis, a similar tool could be developed by training the NN on displacement fields or stress-related quantities, depending on the structural response of interest. In general, any relevant structural parameter can be included as an input or output of the NN model. Future work should focus on the following activities:

- Further investigations on the proper encoding of input parameters to the NN are needed to include as many physical characteristics as possible, e.g., local boundary conditions, anisotropic materials, nonlinear properties.
- The effect of uncertainties on the structural modeling could be significant and should be investigated, e.g., using the Gaussian Regression Process [56].
- Another relevant development concerns the application of the methodology to more complex geometries, such as curved cross-sections or beams.
- Finally, the optimization of the three-dimensional distribution of theories will be explored using the node-dependent kinematics approach, which enables assigning different structural theories and sets of DOFs to individual nodes.

Acknowledgements This publication is part of the project PNRR-NGEU which has received funding from the MUR – DM 117/2023.

Author Contributions MP and GC performed the analyses and wrote the main manuscript. All authors contributed to the models employed and reviewed the manuscript.

Funding Open access funding provided by Politecnico di Torino within the CRUI-CARE Agreement.

Data Availability Datasets are available upon request.

Declarations

Conflict of interest The authors declare no conflict of interest.

Open Access This article is licensed under a Creative Commons Attribution 4.0 International License, which permits use, sharing, adaptation, distribution and reproduction in any medium or format, as long as you give appropriate credit to the original author(s) and the source, provide a link to the Creative Commons licence, and indicate if changes were made. The images or other third party material in this article are included in the article's Creative Commons licence, unless indicated otherwise in a credit line to the material. If material is not included in the article's Creative Commons licence and your intended use is not permitted by statutory regulation or exceeds the permitted use, you will need to obtain permission directly from the copyright holder. To view a copy of this licence, visit http://creativecommons.org/licenses/by/4.0/.

References

1. Carrera, E., Petrolo, M.: On the effectiveness of higher-order terms in refined beam theories. J. Appl. Mech. **78**(2), 021013 (2010). (**11**)
2. Euler, L.: Lausanne and Geneva: Bousquet, (1744). (De curvis elasticis)
3. Timoshenko, S.P.: On the transverse vibrations of bars of uniform cross-section. Lond. Edinb. Dublin Philos. Mag. J. Sci. **43**(253), 125–131 (1922)
4. Timoshenko, S.P.: On the correction for shear of the differential equation for transverse vibrations of prismatic bars. Lond. Edinb. Dublin Philos. Mag. J. Sci. **41**(245), 744–746 (1921)
5. Mittelstedt, C.: Generalized beam theory for the analysis of thin-walled structures—a state-of-the-art survey. Thin-Wall. Struct. **200**, 111849 (2024)
6. Yu, W., Hodges, D.H., Ho, J.C.: Variational asymptotic beam sectional analysis—an updated version. Int. J. Eng. Sci. **59**, 40–64 (2012). (**The Special Issue in honor of Victor L. Berdichevsky**)
7. Ma, W., Li, X.: A higher-order beam theory for analyzing the static and dynamic behaviors of box and tubular beam-columns with the higher-order effect of axial force. Acta. Mech. Sin. **42**(3), 524391 (2026)
8. Latalski, J., Zulli, D.: Generalized beam theory for thin-walled beams with curvilinear open cross-sections. Appl. Sci. **10**(21), 7802 (2020)
9. Choi, S., Kim, Y.: Consistent higher-order beam theory for thin-walled box beams using recursive analysis: edge-bending deformation under doubly symmetric loads. Eng. Struct. **206**, 110129 (2020)
10. Kim, J., Choi, S., Kim, Y., Jang, G.-W.: Hierarchical derivation of orthogonal cross-section modes for thin-walled beams with arbitrary sections. Thin-Wall. Struct. **161**, 107491 (2021)
11. Choi, S., Kim, J., Jeon, J., Chang, H., Park, J.C., Kim, Y., Jang, G.-W.: Higher-order modeling of a thin-walled beam with a welded multicell cross-section and its application to welding line optimization. Comput. Struct. **283**, 107056 (2023)
12. Ma, W.-L., Jiang, Z.-C., Lee, K.-Y., Li, X.-F.: A refined beam theory for bending and vibration of functionally graded tube-beams. Compos. Struct. **236**, 111878 (2020)
13. Turan, F.: Lateral-torsional buckling of porous orthotropic thin-walled i-beams under non-uniform transverse loadings: a

higher-order shear deformation approach. Int. J. Mech. Mater. Des. **22**(1), 37 (2026)
14. Zhang, R., Mo, S., Yao, X.: A geometrically exact higher order beam model and its weak form quadrature element formulation. Int. J. Solids Struct. 113579 (2025)
15. Amabili, M.: An accurate model for nonlinear forced vibrations of higher-order and timoshenko cantilever beams. Compos. Struct. 120035 (2026)
16. Yildiz, T., Kabave, K.S., Esen, I.: Vibration simulation of sandwich nano-smart plate with an auxetic core and piezo-electromagnetic face layers based on sinusoidal higher-order theory. Arab. J. Sci. Eng. **50**(22), 18377–18401 (2025)
17. Vindigni, C.R., Mantegna, G., Orlando, C., Alaimo, A., Berci, M.: A refined aeroelastic beam finite element for the stability analysis of flexible subsonic wings. Comput. Struct. **307**, 107618 (2025)
18. Campagna, D., Benedetti, I., Gulizzi, V.: Variable-order framework for aeroelastic flutter analysis of laminated composite wings. Compos. Struct. **371**, 119508 (2025)
19. Campagna, D., Gulizzi, V., Benedetti, I.: A DG-VLM framework for computational static aeroelastic analysis of composite wings. Compos. Struct. **353**, 118697 (2025)
20. Shang, L., Xia, P., Zhang, J., Lin, C.: Geometrically exact aeroelastic stability analysis of helicopter composite rotor blades in forward flight. Aerosp. Sci. Technol. **144**, 108818 (2024)
21. Carrera, E., Cinefra, M., Petrolo, M., Zappino, E.: Finite Element Analysis of Structures Through Unified Formulation. Wiley, Oxford (2014)
22. Petrolo, M., Carrera, E.: Best theory diagrams for multilayered structures via shell finite elements. Adv. Model. Simul. Eng. Sci. **6**, 4 (2019). (**03**)
23. Petrolo, M., Carrera, E.: Best spatial distributions of shell kinematics over 2D meshes for free vibration analyses. Aerotecn. Missili Spazio **99**, 05 (2020)
24. Carrera, E., Miglioretti, F., Petrolo, M.: Computations and evaluations of higher-order theories for free vibration analysis of beams. J. Sound Vib. **331**(19), 4269–4284 (2012)
25. Kudela, J., Matousek, R.: Recent advances and applications of surrogate models for finite element method computations: a review. Soft. Comput. **26**(24), 13709–13733 (2022)
26. Yang, Q., Zhang, L., Zhu, W.: A review of advanced modeling methods for thin-walled beams: from deductive methods to data-driven approaches. Arch. Comput. Methods Eng. (2026)
27. Zaparoli, C.B., Droz, C., Zine, A.M., Foulard, S., Ichchou, M.: A review of machine learning methods applied to structural dynamics and vibroacoustic. Mech. Syst. Signal Process. **200**, 110535 (2023)
28. Thai, H.-T.: Machine learning for structural engineering: a state-of-the-art review. Structures **38**, 448–491 (2022)
29. Wu, R.-T., Jahanshahi Mohammad, R.: Deep convolutional neural network for structural dynamic response estimation and system identification. J. Eng. Mech. **145**(1), 04018125 (2019)
30. Nath, D., Ankit Neog, D.R., Gautam, S.S.: Application of machine learning and deep learning in finite element analysis: a comprehensive review. Arch. Comput. Methods Eng. 1–40 (2024)
31. Meethal, R.E., Kodakkal, A., Khalil, M., Ghantasala, A., Obst, B., Bletzinger, K., Wüchner, R.: Finite element method-enhanced neural network for forward and inverse problems. Adv. Model. Simul. Eng. Sci. **10**(1), 6 (2023)
32. Bolandi, H., Li, X., Salem, T., Boddeti, V.N., Lajnef, N.: Bridging finite element and deep learning: High-resolution stress distribution prediction in structural components. Front. Struct. Civ. Eng. **16**(11), 1365–1377 (2022)
33. Lee G., Lee J.W.: Artificial neural network model to extract modal participation factors for damage localization in beam-like structures. Journal of Mechanical Science and Technology, pages 1–13, (2025)
34. Pagani, A., Enea, M., Carrera, E.: Component-wise damage detection by neural networks and refined fes training. J. Sound Vib. **509**, 116255 (2021)
35. Lee, S., Kim, H., Lieu, Q.X., Lee, J.: CNN-based image recognition for topology optimization. Knowl.-Based Syst. **198**, 105887 (2020)
36. Torregrosa, A.J., Gil, A., Quintero, P., Cremades, A.: A reduced order model based on artificial neural networks for nonlinear aeroelastic phenomena and application to composite material beams. Compos. Struct. **295**, 115845 (2022)
37. Lin, M., Guo, S., He, S., Li, W., Yang, D.: Structure health monitoring of a composite wing based on flight load and strain data using deep learning method. Compos. Struct. **286**, 115305 (2022)
38. Miranda, M., Li, R., Iorga, L., Pinho, S.T.: Multiscale modelling strategy for a novel wingbox structure with increased bend-twist coupling. Compos. Struct. **370**, 119291 (2025)
39. Zobeiry, N., Humfeld, K.D.: A physics-informed machine learning approach for solving heat transfer equation in advanced manufacturing and engineering applications. Eng. Appl. Artif. Intell. **101**, 104232 (2021)
40. Marcinkevičs, R., Vogt, J.E.: Interpretable and explainable machine learning: a methods-centric overview with concrete examples. Wiley Interdiscip. Rev. Data Min. Knowl. Discov. **13**(3), e1493 (2023)
41. Yossef, M., Noureldin, M., Alqabbany, A.: Explainable artificial intelligence framework for frp composites design. Compos. Struct. **341**, 118190 (2024)
42. Azad, M.M., Kim, H.S.: An explainable artificial intelligence-based approach for reliable damage detection in polymer composite structures using deep learning. Polym. Compos. **46**(2), 1536–1551 (2025)
43. Sze, V., Chen, Y.-H., Yang, T.-J., Emer, J.S.: Efficient processing of deep neural networks: a tutorial and survey. Proc. IEEE **105**(12), 2295–2329 (2017)
44. Pasupa, K., Sunhem, W.: A comparison between shallow and deep architecture classifiers on small dataset. In 2016 8th International Conference on Information Technology and Electrical Engineering (ICITEE), pp. 1–6. IEEE (2016)
45. Carrera, E., Pagani, A., Petrolo, M.: Classical, refined, and component-wise analysis of reinforced-shell wing structures. AIAA J. **51**(5), 1255–1268 (2013)
46. Petrolo, M., Pagani, A., Carrera, E., Candita, G., Iannotti, P.: Mapping beam cross-section features to higher-order generalized variables using machine learning. Thin-Wall. Struct. 114108 (2025)
47. Petrolo, M., Iannotti, P., Trombini, M., Pagani, A., Carrera, E.: A machine learning approach to evaluate the influence of higher-order generalized variables on shell free vibrations. J. Sound Vib. **575**, 118255 (2024)
48. Petrolo, M., Iannotti, P.: Best kinematics for shell finite elements using convolutional neural networks. Mech. Adv. Mater. Struct. **30**(5), 1106–1116 (2023)
49. Bathe, K.-J.: Finite Element Procedures (2006)
50. Lin, J.-W.: Artificial neural network related to biological neuron network: a review. Adv. Stud. Med. Sci. **5**(1), 55–62 (2017)
51. Sarker, I.H.: Machine learning: algorithms, real-world applications and research directions. SN Comput. Sci. **2**(3), 160 (2021)
52. Carrera, E., Petrolo, M., Nali, P.: Unified formulation applied to free vibrations finite element analysis of beams with arbitrary section. Shock. Vib. **18**(3), 485–502 (2011)
53. Carrera, E., Giunta, G., Nali, P., Petrolo, M.: Refined beam elements with arbitrary cross-section geometries. Comput. Struct. **88**(5–6), 283–293 (2010)
54. Pastor, M., Binda, M., Hararik, T.: Modal assurance criterion. Procedia Eng. **48**, 543–548 (2012). (**Modelling of Mechanical and Mechatronics Systems**)

55. Allemang, R.J.: The modal assurance criterion-twenty years of use and abuse. Sound Vib. **37**(8), 14–23 (2003)
56. Zamani, D., Pagani, A., Petrolo, M., Carrera, E.: Multi-fidelity probabilistic failure onset analysis of composite structures under uncertainties. Comput. Methods Appl. Mech. Eng. **454**, 118849 (2026)

Publisher's Note Springer Nature remains neutral with regard to jurisdictional claims in published maps and institutional affiliations.